J. Fluid Mech. (2006), *vol.* 555, *pp.* 321–352.
doi:10.1017/S0022112006009232 Printed in the United Kingdom

Modulation of surface flow and vortex shedding of a circular cylinder in the subcritical regime by a self-excited vibrating rod

By R. F. HUANG, J. M. CHEN AND C. M. HSU

Department of Mechanical Engineering, National Taiwan University of Science and Technology, Taipei, Taiwan 10672

(Received 18 February 2005 and in revised form 20 August 2005)

The surface flow, pressure distributions, and vortex-shedding properties of the circular cylinder flow in the subcritical regime modulated by a self-excited vibrating rod were experimentally studied in a closed-circuit wind tunnel for Reynolds numbers between 2×10^4 and 1.8×10^5. The principle of galloping was employed to induce self-vibration of an elastic rod. The natural (uncontrolled) boundary layer showed significantly different flow patterns in two subranges of Reynolds number: $Re_D < 0.55 \times 10^5$ and $Re_D > 0.55 \times 10^5$. In the low-Reynolds-number subrange, the *laminar separation mode*, which was similar to the result reported by previous investigators, was observed. While in the high-Reynolds-number subrange, the *separation bubble mode*, which was rarely discussed previously, was found. The term separation bubble mode was used to denote the existence of secondary recirculation bubbles induced by the reattachment of separated boundary layers. The surface flow modulated by the vibrating rod presented complex variations in these two subranges. Depending on the position of the control rod, the separation bubble mode or the turbulent separation mode might appear because of the increase of the turbulence kinetic energy. Modulating the surface flow patterns could significantly influence the surface pressure distributions on the main cylinder and the vortex shedding in the wake. Forcing the boundary layer at the positions upstream of the natural separation point would drastically lower the values of the minimum pressure coefficient and the base pressure coefficient, and therefore increase the lift. The drag coefficient, however, would not be apparently decreased. The frequency of the vortex shedding in the wake could 'lock' to the rod vibration frequency if the position of the vibrating rod was properly adjusted.

1. Introduction

Numerous studies have been carried out to investigate the aerodynamic characteristics of a circular cylinder which is one of the most basic shapes of bluff bodies used in work on fluid dynamics. When a flow goes across a circular cylinder, complex flow phenomena and behaviours in the vicinity of the cylinder surface and the wake region, e.g. flow separation, vortex shedding and shear-layer instability etc., are usually induced in different regimes of Reynolds numbers. These flow phenomena would inevitably apply steady/unsteady lift and drag forces to the cylinder. Some flow-control methods for modulating the surface flows and the vortex shedding in the wake of a cylinder and subsequently for the alteration of the lift/drag forces can be found in the literature. The following paragraphs briefly review the cylinder flow, the rod-controlled cylinder flow and the motivation for this study.

Term of flow	Range of Reynolds number	Important flow properties
Cripping flow	$Re_D < 5$	Symmetric flow
Standing vortices	$5 \approx 15 < Re_D < 45$	A pair of standing vortices appears behind cylinder
Laminar vortex shedding	$45 < Re_D < 150 \sim 300$	(i) Boundary layers on cylinder are laminar (ii) Shed vortices are inherently laminar (iii) Strouhal number St_D increases nonlinearly with increases of Re_D
Subcritical regime	$300 < Re_D < 2 \times 10^5$	(i) Shed vortices are accompanied with turbulent fluctuations (ii) $St_D \approx 0.21$ (iii) Drag coefficient $C_D \approx 1 - 1.2$
Critical regime	$2 \times 10^5 < Re_D < 3 \times 10^5$	(i) Boundary layers on cylinder surface are in transition from laminar to turbulent state (ii) St_D increases abruptly with increase of Re_D (iii) C_D decreases abruptly with increase of Re_D
Supercritical regime	$3 \times 10^5 < Re_D < 10^6$	(i) Boundary layers on cylinder are turbulent with separation bubbles (ii) Strouhal number $St_D \approx 0.48$ (iii) Drag coefficient $C_D \approx 0.22$
Transitional regime	$10^6 < Re_D < 3.5 \times 10^6$	(i) St_D decreases first then increases with increase of Re_D (iii) C_D increases with increases of Re_D
Transitional regime	$3.5 \times 10^6 < Re_D$	(i) Separation bubbles disappear (ii) Strouhal number St_D approaches to 0.28 (iii) Drag coefficient $C_D \approx 0.52$

TABLE 1. Characteristics of circular cylinder flow in different regimes of Reynolds number.

1.1. *Natural cylinder flows*

Studies on flow across a cylinder have been reviewed by, for example, Roshko (1954), Zdravkovich (1997) and Williamson (1997). Roshko traced back the motivation for people to study this topic to curiosity about aeolian tones. He also classified the periodic wake phenomena behind circular cylinders into two distinct Reynolds-number regimes (joined by a transition range), i.e. a stable range for $50 < Re_D < 150$, a transition range for $150 < Re_D < 300$, and an irregular range for $300 < Re_D < 10\,000$ or above. In the stable range, the classical stable Kármán streets are formed; in the irregular range, the periodic shedding is accompanied by irregular, or turbulent, velocity fluctuations.

Flow characteristics in different Reynolds-number regimes have been studied by many investigators (e.g. Roshko 1961; Lienhard 1966; Achenbach 1968; Bearman 1969; Zdravkovich 1969, 1981; Farell & Blessmann 1983; Williamson 1988; Niemann & Hölscher 1990; Nishimura & Taniike 2001; Schewe 2001). Table 1 summarizes the commonly recognized flow characteristics in different Reynolds-number regimes. In table 1, the Reynolds number is defined as $Re_D \equiv uD/\nu$, where u represents the free-stream velocity, D is the diameter of the circular cylinder, and ν is the kinematic

viscosity of the approaching stream. The Strouhal number is defined as $St_D \equiv f_s D/u$, where f_s denotes the frequency of vortex shedding in the cylinder wake. The drag coefficient is defined as $C_D \equiv F_D/(0.5\rho u^2 D)$, where F_D denotes the drag force per unit length of cylinder in the free-stream direction and ρ is the density of the free stream. It is obvious that more characteristic flow regimes were found at high Reynolds numbers. The behaviours of boundary layers and wake instabilities display complex variations in different characteristic flow regimes. The free-stream turbulence also affects the flow properties. Norberg (1986) and Norberg & Sunden (1987) reported the effects of the free-stream turbulence on the vortex shedding and the fluid forces of a single cylinder in crossflow at Reynolds-number ranges of $2 \times 10^4 \sim 6 \times 10^4$ and $2 \times 10^4 \sim 3 \times 10^5$, respectively.

The flow characteristics in the subcritical regime were most widely studied. At subcritical Reynolds numbers, the laminar boundary layers separate from the surface of the cylinder on the front of the cylinder (Roshko 1961). Diverse results of the measured separation point are found in the literature. For instance, Achenbach (1968) found that the boundary layer separates laminarly from the cylinder surface at an angle $\theta = 78^\circ$ measured from the front stagnation point of the circular cylinder at $Re_D = 10^5$ (the angle θ is hereinafter called the separation angle). He obtained this value of separation angle by locating the critical position on the cylinder surface with zero skin friction. Son & Hanratty (1969) applied an electrochemical technique to check for the separation at various Reynolds numbers. They found that the separation angle θ decreases from 85° to 75° when the Reynolds number was increased from 3×10^3 to 10^5. They also found that the results are comparable with the results of Fage & Falkner (1931). Ballengee & Chen (1971) employed the dual-element hot-film probe to determine the separation point by varying the Reynolds number from 10^4 to 4.5×10^4. They found that the separation angle θ moves from 91.5° to 83° as the Reynolds number increases from 10^4 to 4.5×10^4. Lee & Basu (1997) employed the multiple hot-film sensor array and surface pressure measurement techniques for the Reynolds-number range between 2.4×10^4 and 5.1×10^4. They found an 82.5° separation angle at $Re_D = 4 \times 10^4$. Nishimura & Taniike (2001) located the inflection point of the surface pressure distribution and found that the time-averaged separation angle at $Re_D = 6.1 \times 10^4$ is 76.2°. Alam *et al.* (2003) found that the time-averaged flow separation angle is about 75° at $Re_D = 6.5 \times 10^4$. Apparently, the separation angles measured by investigators are widely diverse, even in the same Reynolds-number range.

The surface flow in the subcritical regime was generally taken as a 'simple' laminar separation, as indicated by, for example, Zdravkovich *et al.* (1989), Niemann & Hölscher (1990), Tsutsui & Igarashi (2002), and Alam *et al.* (2003). The word 'simple' means that a single separation point exists on each side of the cylinder so that the flows along the leeward surface downstream of the separation point are reversed. The time-averaged flow pattern in the wake of the cylinder should display a pair of standing recirculation bubbles. Gölling, Dallmann & Kreplin (2000) pointed out the possible existence of two separation points on either side of the cylinder at Reynolds numbers around the upper boundary of the subcritical regime; however, detailed measurements were not shown.

1.2. *Flow control using a small static cylinder*

In order to reduce the drag and suppress the periodic forces induced by the surface-flow separation and vortex shedding, some static passive flow-control methods have been proposed and investigated to modulate the surface flows and the vortex shedding

of the cylinder flows. Zdravkovich (1981) classified the practically effective surface-flow control methods into surface protrusions, shrouds and near-wake stabilizers. The control methods, however, generally worked in a limited range of Reynolds numbers. Strykowski & Sreenivasan (1990) reported that by properly placing a small control cylinder in the near-wake shear layer of a main cylinder (no farther than approximately 3.5 to 4 diameters downstream of the main cylinder), the vortex shedding of the main cylinder can be dramatically suppressed for the flows at Reynolds numbers up to 80. It was argued that the properly placed control cylinder weakens the shear layer by spreading the velocity gradient over a larger distance, i.e. diffusing vorticity. When the control cylinder was placed farther outside, but near the locus of maximum vorticity, the wake of the control cylinder was most effective in reducing the circulation in that portion of the shear layer which was most critical for vortex formation. If the circulation was reduced below some threshold level in the formation region, the mutual attraction between the opposing shear layers would be too weak to form the vortex roll-ups. In other words, the presence of the control cylinder had the effect of altering the local instability of the flow by smearing and diffusing concentrated vorticity in the shear layers behind the body; a related effect was that the control cylinder diverts a small amount of fluid into the wake of the main cylinder.

Sakamoto, Tan & Haniu (1991) installed a small circular cylinder near the separated shear layer on one side of a square prism and found that the maximum reduction in the time-mean and fluctuating drags occurred when the control cylinder was located near what would ordinarily be considered the outer boundary of the shear layer at Reynolds numbers of 4.2×10^4 and 6.5×10^4. Sakamoto & Haniu (1994) placed a small control cylinder in either the upstream or downstream region of a main cylinder and found that vortex shedding can be effectively suppressed.

Prasad & Williamson (1997) and Tsutsui & Igarashi (2002) placed a control rod upstream of the main cylinder along the central axis. By adjusting the distance between the control and the main cylinders, they found a wake-impingement mode that can significantly reduce the time-mean and the dynamic drags for the Reynolds-number range between 1.5×10^4 and 6.2×10^4.

1.3. *Ideas of flow control using a self-excited vibrating rod*

When a flow goes across an elastic structure, the mutual interaction among the induced aerodynamic forces, the elastic forces, and the inertial forces should be taken into consideration because of its significant contributions to the stability of the structure. Since, for a given configuration of the elastic body, the aerodynamic forces increase rapidly with the crossflow speed, while the elastic stiffness is independent of the crossflow, there may be a critical crossflow speed at which the structure becomes unstable. The phenomena of flutter, galloping and vortex-induced vibration are typical examples of the structural instabilities corresponding to the wings of airplane, ice-coated power lines and two-dimensional long cylinders, respectively. These phenomena were discussed in work on *aeroelasticity* (Fung 1969; Dowell 1978). We use the galloping phenomenon of the structure to make a small-diameter rod generate self-excited vibration so that the boundary layer of the main circular cylinder can be influenced.

Two typical examples of the galloping phenomenon can be found in the classic text books on aeroelasticity: the uniform flow passing over an elastic cylinder with an asymmetric cross-section; and the shear flow across a circular cylinder (figure 1). In figure 1(*a*), a flow of uniform velocity u_w passes over a two-dimensional elastic cylinder with an asymmetric cross-section. Let C_L and C_D be experimentally determined steady

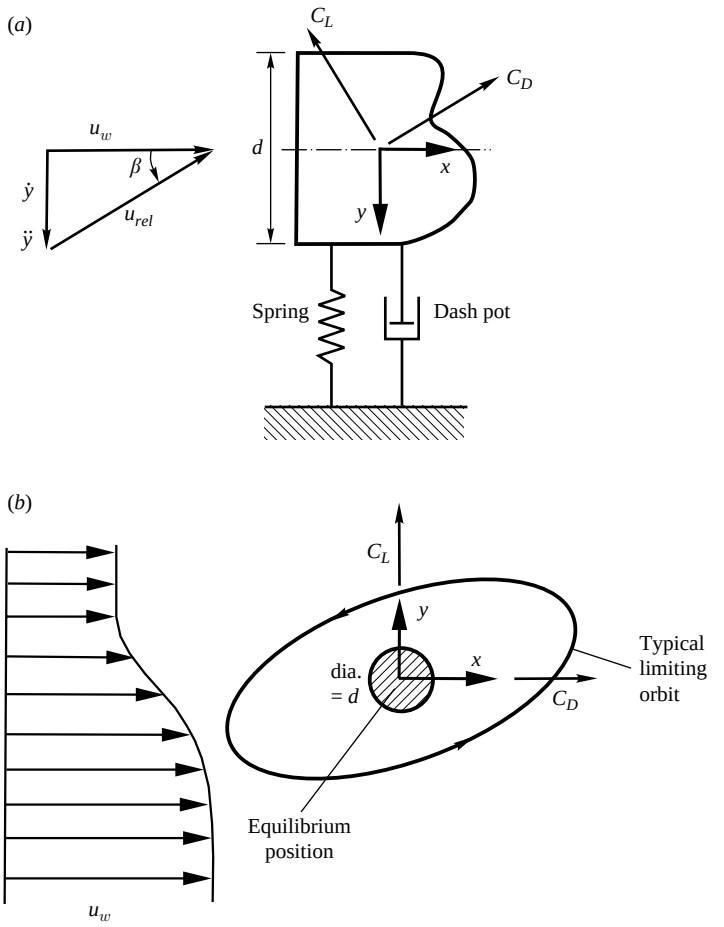

FIGURE 1. Schematic diagrams showing typical examples of galloping analysis.

lift and drag coefficients, respectively, of the section given as functions of the relative angle of attack β of the crossflow. The crossflow displacement is denoted as y, the velocity downward is $\dot{y}$, the acceleration is $\ddot{y}$, and the crossflow velocity relative to the moving section is denoted as u_{rel}. The standard procedure for analysing this kind of problem is to assume a spring/dash pot model (so that the effects of both the elasticity and damping are included for consideration), derive the equation of motion of the section according to the assumed model, engage the aerodynamic lift and drag forces to the source term of the equation of motion, then employ the linear theory of stability to obtain the condition necessary for galloping. The motion of the section in this case in the y direction (y, $\dot{y}$, and $\ddot{y}$) is governed by an equation of motion consisting of all the parameters mentioned above. The system is unstable if the coefficient of the damping term (the $\dot{y}$ term) in the equation of motion goes towards negative values. Den Hartog (1956) used the standard method mentioned above to derive a critical criterion ($\mathrm{d}C_L/\mathrm{d}\alpha + C_D < 0$) for the condition necessary for galloping for the case of figure 1(*a*). In the case of figure 1(*b*), a shear flow with a free-stream velocity u_w goes across a circular cylinder. Simpson (1971) derived the equations of motion for this system for both the x- and y-directions. Assuming a small amplitude of instability motion, the equations of motion were linearized and solved by assuming the solution

to have the general form of $e^{\lambda t}$, where $\lambda = \omega_1 + i\omega_2$ and t is the time. In the definition of λ, ω_1 is the real part and ω_2 is the imaginary part of the oscillation frequency. Solutions for x and y of the form $e^{\lambda t}$ are supposed to be unstable (divergent) when the real frequency $\omega_1 > 0$. For $\omega_1 = 0$, boundaries in the shear flow were then defined which identified the regions of shear-layer galloping susceptibility. It was found that the circular cylinder in a shear flow may induce orbiting motions if it is unstable, as shown in figure 1(*b*). Galloping is a phenomenon that designers always try to avoid because it frequently causes breakup of structures. The galloping frequency may not coincide with the natural frequency of the subject.

According to the experiments of Blevins (1990), when a free-stream with a velocity u_w passes over an asymmetric subject with a cross-stream width d and a natural frequency f, galloping (a lift-induced vibration) may occur if the reduced velocity $u_w/fd > 20$. Consider an iron circular rod of diameter $d = 1$ mm and length $L = 520$ mm, clamped at two ends, the resonant frequency f_n of the first, second and third bending modes of the two-ends-clamped iron rod will be 12.7, 34.9 and 68.4 Hz, respectively (Rao 1995). If the approaching free-stream velocity u_w is moderate, say, $15\,\mathrm{m\,s^{-1}}$, then the vortex-shedding frequency, f_s, of the static circular rod of diameter 1 mm should be 5312 Hz by considering the Strouhal number of the rod to be about 0.21 (Blevins 1990). The vortex shedding would not induce resonance of the rod because it is much higher than the natural frequencies of the rod and does not coincide with any of the harmonics of the resonant frequencies. If the iron rod is placed near a cylinder of diameter D, a shear-flow (non-uniform velocity distribution) may be induced when the stream approaches the rod because of the existence of the cylinder. Consequently, a lift force acting on the control rod must be induced. At the wind velocity $u_w = 15\,\mathrm{m\,s^{-1}}$, the reduced velocity u_w/fd would be about 880, which is much greater than the critical value 20 (Blevins 1990). Thus, it possible to induce galloping of the rod.

Using a static rod to control the flow across a circular cylinder has been studied as mentioned above (e.g. Strykowski & Sreenivasan 1990). The investigators showed that the static rod placed near the cylinder could modify the symmetric flow field and influence the surface flow and the vortex-shedding properties. The effective regime of the Reynolds number reported by Strykowski & Sreenivasan was up to 80, which was in the range of laminar vortex-shedding. In order to study the possibility of extending the effective range of the flow control to the subcritical regime ($300 < Re_D < 2 \times 10^5$), the static-rod method was substituted by a vibrating rod in this study. A passive control method which used the phenomenon of galloping to cause self-vibration of an elastic rod was developed. The self-excited vibrating rod was placed near the circular cylinder. The surface flow patterns, the surface pressure distributions, and the vortex-shedding properties of the natural and the controlled cylinders in the subcritical regime were examined and compared to see the effects induced by the rod agitation in the boundary layer.

2. Experimental arrangements

2.1. *Test rig*

The circular cylinder and the control rod were installed in a wind-tunnel test section, as shown in figure 2. The wind tunnel was of the closed-return type, which had a test section of $60 \times 60 \times 120\,\mathrm{cm^3}$. The free-stream turbulence intensity was less than 0.2 % in the wind speed range 5–$45\,\mathrm{m\,s^{-1}}$. The average velocity of the approaching flow was determined with a Pitot static tube. A hollow circular cylinder made of

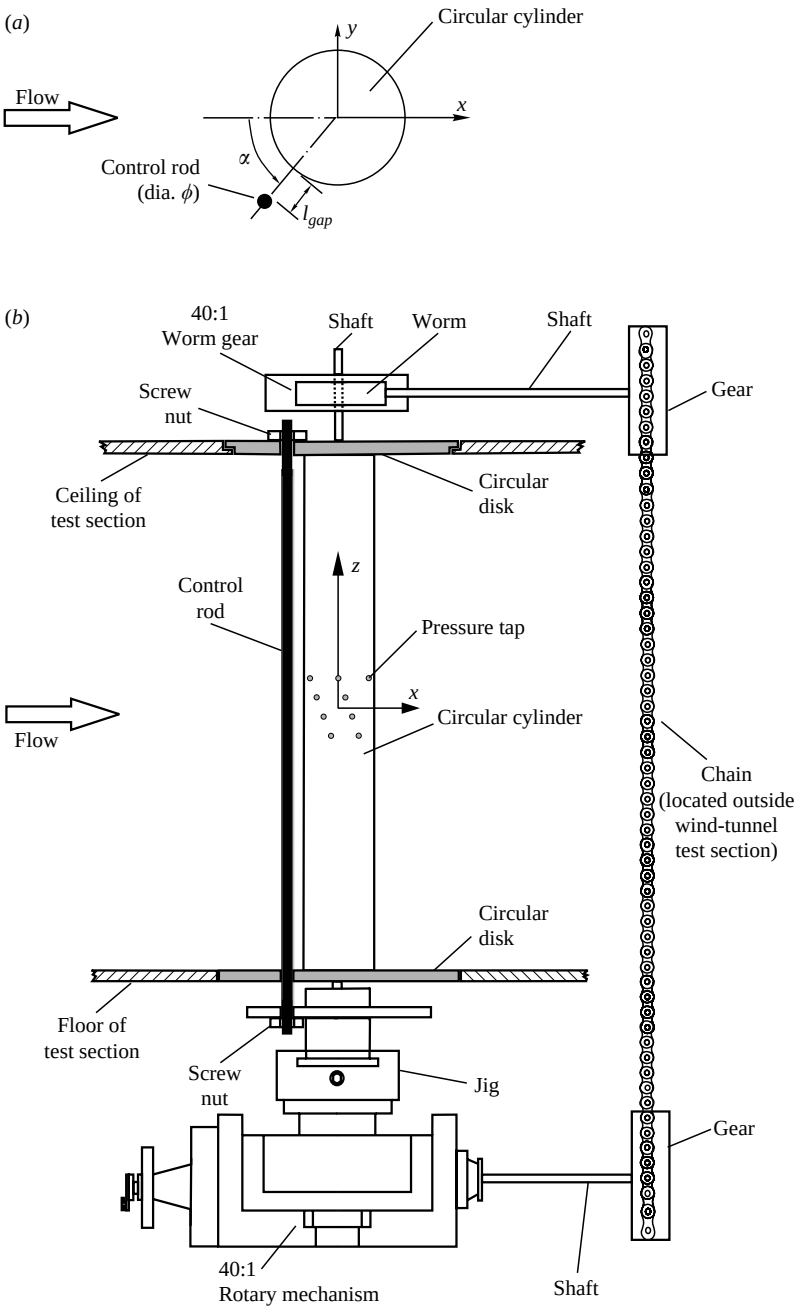

FIGURE 2. Experimental set-up. (*a*) Top view; (*b*) side view.

aluminium alloy (6061TET62) with an outer diameter $D = 6$ cm and a length $L = 60$ cm was mounted vertically on a rotary mechanism. The aspect ratio is thus 10. The rotary mechanism has a resolution of 0.0175°. An iron rod of diameter $\phi = 1$ mm was installed vertically and paralleled to the main cylinder at a distance l_{gap} from the main cylinder. The gap distance, l_{gap}, between the rod and the main cylinder could be varied between 1 mm and 3 mm. In the experiment, the gap $l_{gap} = 1$ mm was

found to be most effective for inducing rod vibration. For $l_{gap} > 1$ mm, the vibration of the rod was weak or diminished. Therefore, $l_{gap} = 1$ mm was adopted in this study. A specially designed mechanism was used to connect the rod, the main cylinder, and the rotation support so that they could rotate simultaneously without any shift in relative positions. The angle α could be varied freely by rotating the assembly of the main cylinder and the rod. The rod presented a self-excited transverse vibration when it was placed close to the main cylinder in some ranges of α and l_{gap}. The vibration frequency of the rod could be regulated by adjusting the tightness (tension) of the rod via the screw nuts at both ends of the rod.

2.2. *Pressure sensing*

Thirty-two pressure taps were made and evenly distributed around the periphery of the central section of the main cylinder in four rows (figure 3). The diameter of the tap hole was 1 mm, and the spacing between two neighbouring taps was 11.25°. For each tap, a short stainless steel tube was inserted tightly into the tap hole from the inside of the hollow cylinder and subsequently connected to a plastic polyester tube. The polyester tube was led through a hole located at the top end-cap of the cylinder and connected to a home-made pressure scanner. The pressure signals were transmitted through the taps, the small-diameter stainless steel tubing, the polyester tubing, and finally reached the computer-based pressure scanner. The pressure scanner used a personal computer and a logic circuit to control the states (on/off) of 32 electromagnetic valves. The electromagnetic valves may be open and closed one-after-another at preset through-time, shut-off time and scanning rate. The pressure sensor was a piezoelectric type with a full scale of ± 127 mm Aq. It was constantly calibrated with a micro-pressure calibrator to an uncertainty of 0.01 mm Aq. The output analogue signals ($-10 \sim 10$ V corresponding to the full scale of pressure measurement range) of the pressure sensor were sampled by a PC-based data acquisition system. The data acquisition system had a resolution of 12 bits. The data acquisition system was frequently calibrated to an uncertainty smaller than 1 mV. In this study, the through-time, shut-off time, and the scanning rate of the pressure scanner were set at 20 s, 20 s, and 0.025 Hz, respectively. The data acquisition started at the sixth second of the through-time and lasted for 10 s. The sampling rate and record length were 30 00 Hz and 30 000 samples, respectively.

2.3. *Free-stream velocity detection*

The average free-stream velocity was detected with a retractable Pitot static tube along with a high-precision electronic pressure transducer. In order not to influence the flow field, the Pitot static tube was retracted to the floor of the test section when the velocity measurements were conducted. The operation range of the crossflow Reynolds number based on the cylinder diameter D was between 2×10^4 and 1.8×10^5. The accuracy of the measurement of the free-stream velocity was affected primarily by the alignment of the Pitot tube and the calibration of the pressure transducer. With the help of an on-line micro-pressure calibration system and the careful alignment of the Pitot tube, the uncertainty of the free-stream velocity measurement was estimated to be as large as 3 % of the reading.

2.4. *Detection of rod vibration*

A photoelectric switch was used to detect the vibration frequency of the rod. The photoelectric switch consisted of a 0.75 mm diameter optical fibre transmitter/receiver and a high-response photoelectric amplifier. The optical fibre transmitter/receiver produced a beam of modulated infrared light and received the target-reflected optical

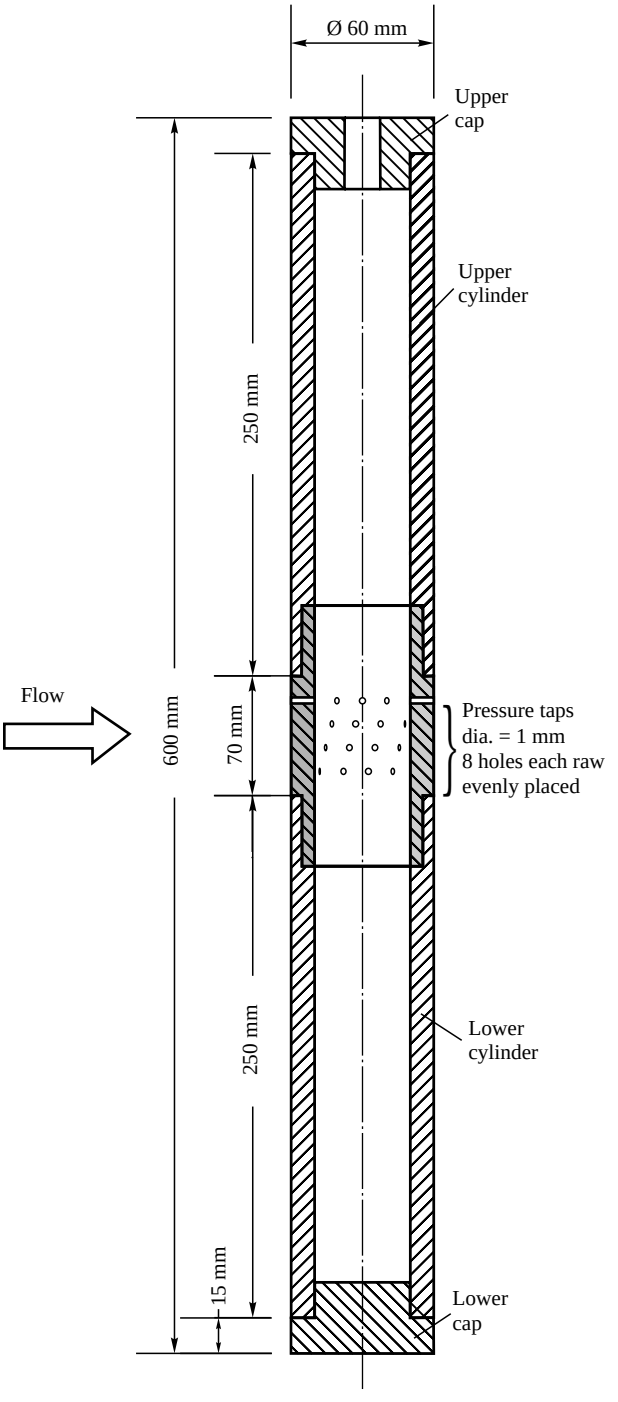

FIGURE 3. Structure of the main cylinder and deployment of pressure taps.

signals. Maximum sensing distance and minimum target size were 15 mm and 0.2 mm, respectively. The photoelectric amplifier had a frequency response up to 20 kHz, which could output a negative square-wave voltage signal when a light-reflective

object passed through the sensitive region of the optical transmitter/receiver. The voltage outputs were fed into a fast Fourier transform (FFT) analyser to extract the vibration frequency of the rod.

2.5. *Surface oil-flow visualization*

The surface oil-flow technique (Huang *et al.* 1996) was employed to detect the characteristic flow patterns. Mineral oil mixed with a small quantity of blue dye powder was brush-coated onto the surface of the main cylinder. The flow direction on the cylinder surface was identified *in situ* from the trace of the oil-flow motion. Dark traces on the cylinder surface were found where the mass of dyed-oil accumulated. Positions of separation and reattachment of the boundary layer on the cylinder surface were taken from the recorded video images of the surface oil-flow patterns. According to the analysis of Squire (1961) and Merzkirch (1974), the uncertainty of identifying the position of the separation point on the cylinder using the surface oil-flow visualization method would be less than 8 % at the free-stream velocity $u_w = 5\,\mathrm{m\,s^{-1}}$. The uncertainty decreased with the increase of the free-stream velocity.

2.6. *Detection of wake instabilities*

The vortical instabilities in the cylinder wake were detected by a home-made constant-temperature one-component hot-wire anemometer. In order to detect properly the frequency of the vortical motions, the probe position was carefully adjusted in the y-direction to capture the oscillation signals. Normally, the probe was placed where the periodical signals revealed local maximum amplitudes. The output signals of the hot-wire anemometer were fed simultaneously to an FFT analyser and a high-speed PC-based data acquisition system. During the experiment, the output signals of the hot-wire anemometer were monitored by using the FFT analyser through the time and frequency domains to ensure the appropriatness of the probe position at all times. The data acquisition system had a sample-and-hold function for multi-channel acquisition without phase-lag. The hot-wire probe used was TSI 1210-T1.5, which could be applied in either endflow or crossflow. The original tungsten wire was replaced by platinum wire. The wire diameter and length were 5 μm and 1.5 mm, respectively. The dynamic response frequency corresponding to the electronic square-wave test was adjusted to 20 kHz. The sampling rate and the elapse time of the data acquisition system were set to 23 000 samples $\mathrm{s^{-1}}$ and $7\,\mathrm{s^{-1}}$, respectively. The accuracy for the hot-wire probe positioning was 10 μm. The accuracy of the shedding-frequency detection depended not only on the response of the hot-wire anemometer, but also on the record length and sampling rate of the FFT analyser. The uncertainty of the frequency detection was estimated to be within ± 0.75 % of the reading in this experiment.

3. Result and discussion

3.1. *Vibration characteristics of the control rod*

Before the experiments are conducted, the vibration characteristics of the iron rod of $\phi = 1$ mm installed at $l_{gap} = 1$ mm are tested at various values of the angle and the Reynolds number Re_D. It is found that the control rod can vibrate only in the range of $50^\circ < \alpha < 100^\circ$ as Re_D varies from 0.2×10^5 to 1.8×10^5, as shown in figure 4. The vibration frequency of the control rod can be modulated by adjusting the tightness of the clamping screw nuts installed at both ends of the rod. The higher the tension

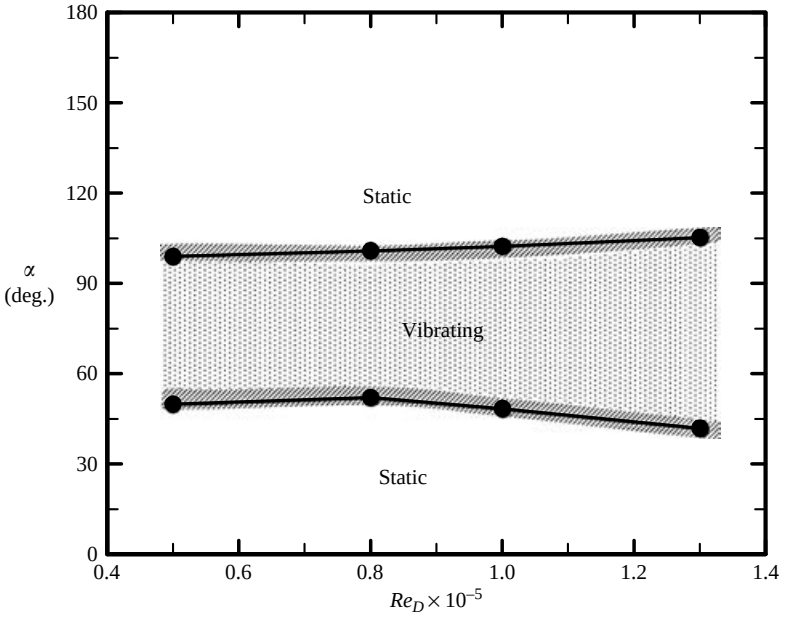

FIGURE 4. Characteristic regimes of rod vibration. Iron rod, $\phi = 1$ mm, $l_{gap} = 1$ mm.

applied to the screw nuts, the larger is the vibration frequency obtained. For instance, at $Re_D = 0.5 \times 10^5$, the vibration frequency f_r may change from 39.25 Hz to 68.75 Hz with the increase of tension applied to the screw nuts. The rod presents large vibration amplitude at low vibration frequency and vice versa. When the clamping screw nuts are fixed at a certain tightness, the vibration frequencies at all Reynolds numbers increase slightly with the increase of α. The vibration frequency also increases with the increase of Reynolds number at a fixed control angle α. The mode shapes of vibration present orbiting characteristics at the midsection, although the orbiting trajectories appear to be different at different Reynolds numbers and rod positions. The following sections are for the clamping screw nuts fixed at a certain tightness.

3.2. *Surface flows of a natural circular cylinder*

Figure 5 shows typical pictures of the dyed-oil flow on the surface of the natural circular cylinder at various Reynolds numbers. According to the observed results, the flow patterns in the range $-4 \leqslant z/D \leqslant 4$ are 'almost two-dimensional' at all experimental Reynolds numbers. Therefore, only the range $-0.5 \leqslant z/D \leqslant 5$ is shown for demonstration. In figure 5(*a*) for $Re_D = 0.3 \times 10^5$, a narrow dark strip appears at the angle $\theta_1 \approx 77^\circ$, where the symbol θ_1 stands for the angle of the upstream edge of the dark oil strip measured from the forward stagnation point of the cylinder. A transparent scale, which is made of polynomial thin film of 15 μm in thickness, is attached to the cylinder surface to assist in the reading of the angle θ_1. The dark strip on the picture indicates where the dyed oil accumulates. The arrows marked on the pictures indicate the visual directions of oil flow on the cylinder surface. Apparently, the boundary layer separates at the location of the dark oil strip because the flow direction downstream of the separation line is reversed. Because the separation point is a three-way saddle towards which the flows on the cylinder surface converge, the oil accumulates there to form the dark strip. In figure 5(*b*) for $Re_D = 0.5 \times 10^5$, the situation is similar to that observed in figure 5(*a*): a separation line appears at

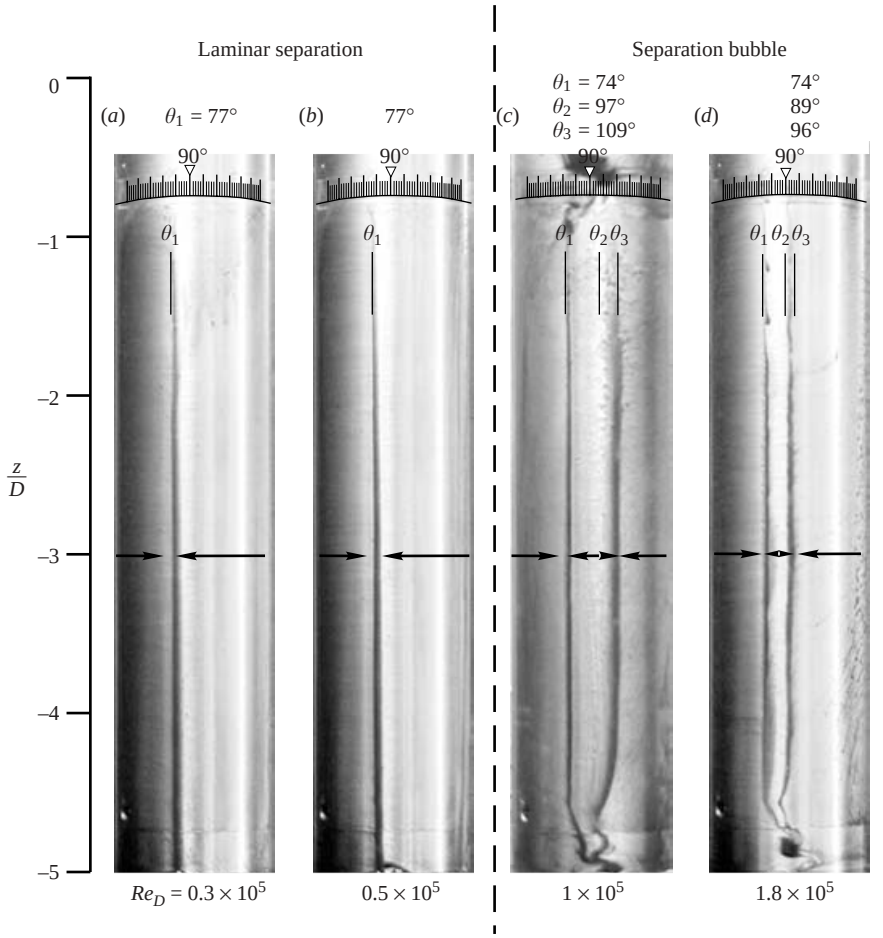

FIGURE 5. Surface oil-flow patterns of a natural (uncontrolled) circular cylinder at various Reynolds numbers. (*a*) $Re_D = 0.3 \times 10^5$, (*b*) 0.5×10^5, (*c*) 1.0×10^5, (*d*) 1.8×10^5.

$\theta_1 \approx 77°$. Surface flow of the above described pattern is termed the laminar separation mode, which is observed at Reynolds numbers lower than about 0.55×10^5.

At Reynolds numbers larger than about 0.55×10^5, the pictures of the surface oil-flow have a different appearance (i.e. two oil-accumulated dark strips) from the laminar separation mode, as shown in figures 5(*c*) and 5(*d*) for $Re_D = 1 \times 10^5$ and 1.8×10^5, respectively. The upstream strip (the left-hand one) is narrower and the downstream strip (the right-hand one) is wider. The symbol θ_1 stands for the angle of the upstream edge of the upstream dark oil strip measured from the forward stagnation point of the cylinder. The symbols θ_2 and θ_3 denote the angles of the upstream and downstream edges, respectively, of the downstream dark strip measured from the forward stagnation point of the cylinder. Because the visual surface oil flow in the region upstream of the upstream dark strip goes downstream and the oil flow in the region downstream of the upstream dark strip goes upstream, the upstream dark strip therefore denotes a separation line. The separation angle θ_1 is approximately equal to 74°, which is smaller than that of the laminar separation mode. In the upstream region near the downstream dark strip, the visual flow direction is difficult to distinguish, partly because of the low flow velocity there. In order to distinguish

the flow direction there, a special local flow-visualization method is employed. When a droplet of titanium chloride ($TiCl_4$) liquid is introduced into the region between the upstream and the downstream dark strips by using a metal wire of 0.2 mm in diameter, the direction of the local flow become observable through the motion of white titanium dioxide (TiO_2) particles (the TiO_2 smoke particles are generated through the chemical reaction $TiCl_4 + 2H_2O \longrightarrow TiO_2 + 4HCl$). It is found that the flow in the upstream region near the downstream dark strip moves downstream and the flow in the region downstream of the dark strip moves upstream, as shown by the arrows in figures 5(*c*) and 5(*d*). Therefore, there is a second separation point existing around the down stream dark strip. The boundary layer separates from the upstream dark strip and should reattach to the cylinder surface at a three-way saddle located between the upstream and downstream dark strips. Because the flows on the cylinder surface must diverge from the reattachment point, the oil does not accumulate to form a dark strip at that point. Therefore, there is no trace of an oil-accumulated pattern appearing between the upstream and downstream dark oil strips. In figure 5(*c*) for $Re_D = 1 \times 10^5$, $\theta_2 \approx 97^\circ$ and $\theta_3 \approx 109^\circ$. The flow pattern shown in figure 5(*d*) for $Re_D = 1.8 \times 10^5$ is similar to that of figure 5(*c*). However, the characteristic angles of surface flow shift to $\theta_2 \approx 89^\circ$ and $\theta_3 \approx 96^\circ$, which indicates that the downstream dark strip moves upstream with the increase of Reynolds number. The strip width also reduces with the increase of Reynolds number. Surface flow of the above described flow pattern, which is observed at Reynolds numbers in the sub-range $Re_D > 0.55 \times 10^5$, is termed the *separation bubble* mode because the separated boundary layer reattaches and a recirculation bubble may exist on the cylinder surface.

The topological flow analysis can be employed to illustrate the flow patterns of figure 5. Following Perry & Fairlie (1974) as well as Chong & Perry (1990), the topological flow pattern is characterized by *critical points*, *separatrices* and *alleyways*. In the topological terminology, a critical point is a point in a flow field where the streamline slope is indeterminate, a separatrix is a streamline which leaves or terminates at a saddle, an alleyway is a passageway between two separatrices. By correctly describing the critical points, separatrices and alleyways, the flow map can be clearly delineated. In the present case, the critical points consist of saddles and nodes.

According to the above flow-visualization results, figures 6(*a*) and 6(*b*) propose the 'two-dimensional' topological flow patterns of the near-wake flows of the circular cylinder of the laminar separation and the separation bubble modes in the subcritical regime. The patterns represent time-averaged flow characteristics because they are obtained from the surface oil-flow patterns, instead of the instantaneous streak-flow patterns. For the laminar separation mode, as shown in figure 6(*a*), a forward stagnation point appears at the upstream edge of the cylinder. It is a three-way saddle and is denoted by S_1'. The oil flows along the surface of the cylinder to about 77° measured from the forward stagnation point S_1', then separates at the three-way saddles S_2' and S_4'. A pair of recirculation bubbles surrounding the nodes N_1 and N_2 must exist so that the surface flow downstream of the separation points S_2' and S_4' is reversed. Because the two-dimensional flow is considered, i.e. the compression or stretching in the axial direction is not effective, the recirculation bubbles surrounding the nodes N_1 and N_2 are represented by the *centres* instead of the *focuses* (Perry & Steiner 1987). Hunt *et al.* (1978) obtained a general formula for the relationship between the numbers of nodes (including four-way nodes N and three-way nodes N') and saddles (including four-way saddles S and three-way saddles S') for the flow around the surface obstacles. The topological rule is $(\sum N + \frac{1}{2}\sum N') - (\sum S + \frac{1}{2}\sum S') = 1 - n$, in which n is the connectivity of the section of the flow under consideration.

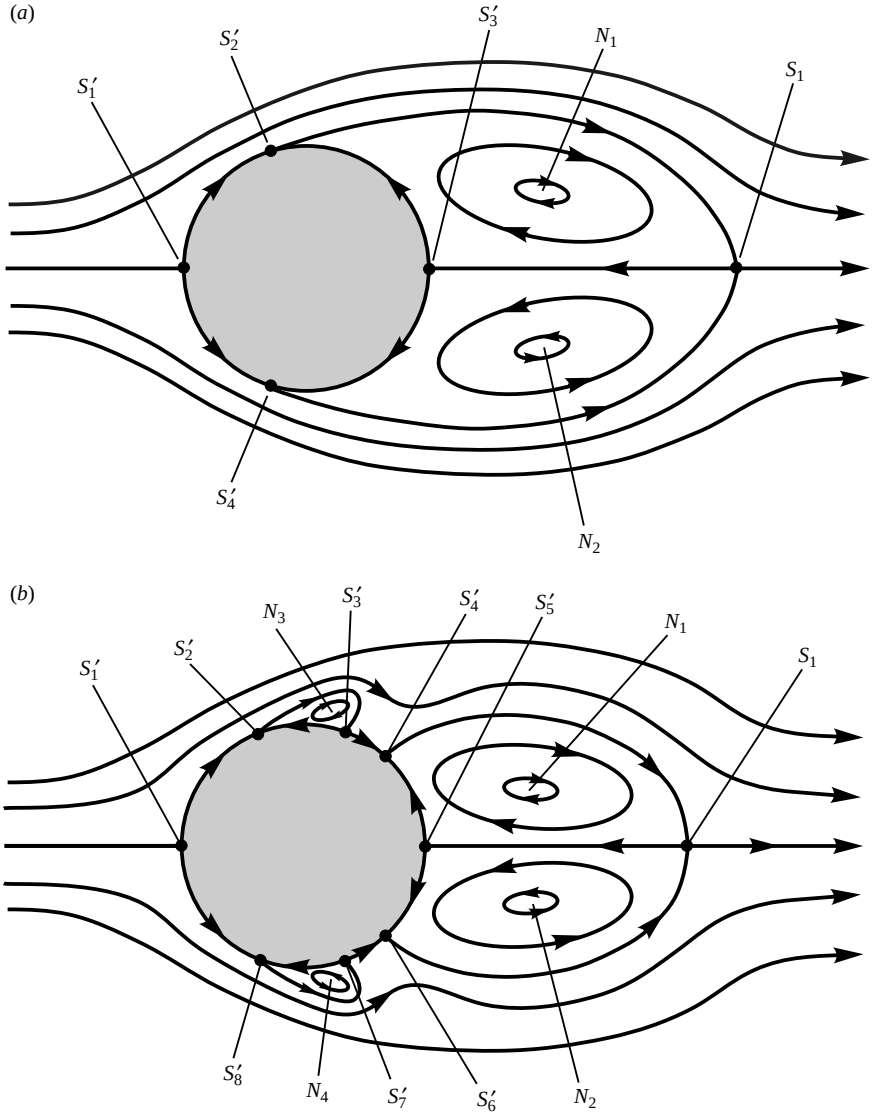

FIGURE 6. Topological flow patterns of a natural circular cylinder for two-dimensional flow. (*a*) Laminar separation for $Re_D < 0.55 \times 10^5$. (*b*) Separation bubble for $Re_D > 0.55 \times 10^5$.

In this case, $n = 2$ because one solid obstacle is present in the flow field. By counting the number of critical points in figure 6(*a*), it is obvious that the topological rule is satisfied because $\sum N = 2$, $\sum N' = 0$, $\sum S = 1$ and $\sum S' = 4$. By referring to the flow directions and separation lines of figures 5(*c*) and 5(*d*), the topological model for the two-dimensional flow of the separation bubble mode is proposed as shown in figure 6(*b*). The small recirculation vortices enclosing the nodes N_3 and N_4 should appear behind the upstream separation points S_2' and S_8' because the separated boundary layers reattach to the three-way saddles S_3' and S_7'. The flows downstream of the reattachment points S_3' and S_7' go downstream and separate at the downstream separation points S_4' and S_6'. Thereafter a pair of counter-rotating recirculation bubbles enclosing the nodes N_3 and N_4 appears in the wake. This

model consists of 4 nodes, 1 four-way saddle and 8 three-way saddles so that $(\sum N + \frac{1}{2}\sum N') - (\sum S + \frac{1}{2}\sum S') = -1$, which satisfies the topological rule.

If the axial compression or stretching effect applies to the flow, i.e. the three-dimensional effect is considered, the large structures in the topological flow patterns would still look similar to those in figure 6 except that the structure of the 'centre' must be replaced by the 'focus'. In substituting the centres by the focuses, some minor flow structures must be modified in order to satisfy the topological rule. Figure 7(*a*) shows the topological flow pattern of the laminar separation mode with consideration of the three-dimensional effect. The centres enclosing the nodes N_1 and N_2 in figure 6(*a*) are replaced by focuses, and the number of nodes and saddles still remains the same. For the separation bubble mode, two possible topological models with consideration of three-dimensional effects are proposed in figure 7(*b*). Type I is simply a modification of figure 6(*b*) by replacing the centres with focuses, whereas type II is another possibility that can still satisfy the topological rule. Two counter-rotating vortex pairs, which enclose the nodes of focuses N_3, N_4, N_5 and N_6, with common vertexes at four-way saddles S_2 and S_3 must exist so that the flow directions on the cylinder surface can follow those in figures 5(*c*) and 5(*d*). This model consists of 6 nodes, 3 four-way saddles and 8 three-way saddles. Therefore, $(\sum N + \frac{1}{2}\sum N') - (\sum S + \frac{1}{2}\sum S') = -1$, which satisfies the topological rule. This type of flow pattern can also be found in the flow-visualization results of an impulsively started circular cylinder towed in a water tank (e.g. Nakayama 1988; Bouard & Coutanceau 1980).

As reviewed in § 1, the surface flow in the subcritical regime is generally taken as a 'simple' laminar separation (e.g. Zdravkovich *et al.* 1989; Niemann & Hölscher 1990; Tsutsui & Igarashi 2002; Alam *et al.* 2003). The word 'simple' refers to a single separation point existing on each side of the cylinder so that the flow along the leeward surface downstream of the separation point is reversed. This 'simple' laminar separation corresponds to the laminar separation mode of figure 6(*a*) or figure 7(*a*), which occurs in the Reynolds number subrange of $Re_D < 0.55 \times 10^5$. However, the time-averaged separation bubble mode of figure 6(*b*) or figure 7(*b*) in the sub-range of $Re_D > 0.55 \times 10^5$ of the subcritical regime was rarely discussed in the literature. It is notable that the time-averaged separation angles measured by investigators are widely diverse, ranging from 75° (Alam *et al.* 2003) to 91.5° (Ballengee & Chen 1971), as discussed in § 1. Niemann & Hölscher (1990) compared many experimental results and argued that their diversity may be caused by different aspect ratios and end conditions of the cylinder, roughness of the cylinder surface, blockage ratio of the wind tunnel or water tunnel, turbulence intensity of the free stream, experimental techniques employed for identification of the separation angle, etc. They concluded that the separation angle in the subcritical regime should be located between 70° and 80° for a circular cylinder with smooth surface, large aspect ratio low blockage ratio, and low turbulence intensity in the free stream. The characteristic angles (θ_1, θ_2 and θ_3) measured in this study are shown in figure 8. In the subrange of laminar separation ($Re_D < 0.55 \times 10^5$), the separation angle θ_1 remains almost 77°. In the subrange of separation bubble ($Re_D > 0.55 \times 10^5$), the separation angle θ_1 remains about 74°. The angles θ_2 and θ_3, which are induced by the secondary bubbles, decrease gradually with the increase in Reynolds number. The existence of the separation bubble may be one of the reasons for such diversity in measurements.

3.3. *Surface flow of controlled cylinder*

Figure 9 shows typical pictures of the dyed-oil flow on the surface of the circular cylinder under the modulation of a vibrating rod at Reynolds number $Re_D =$

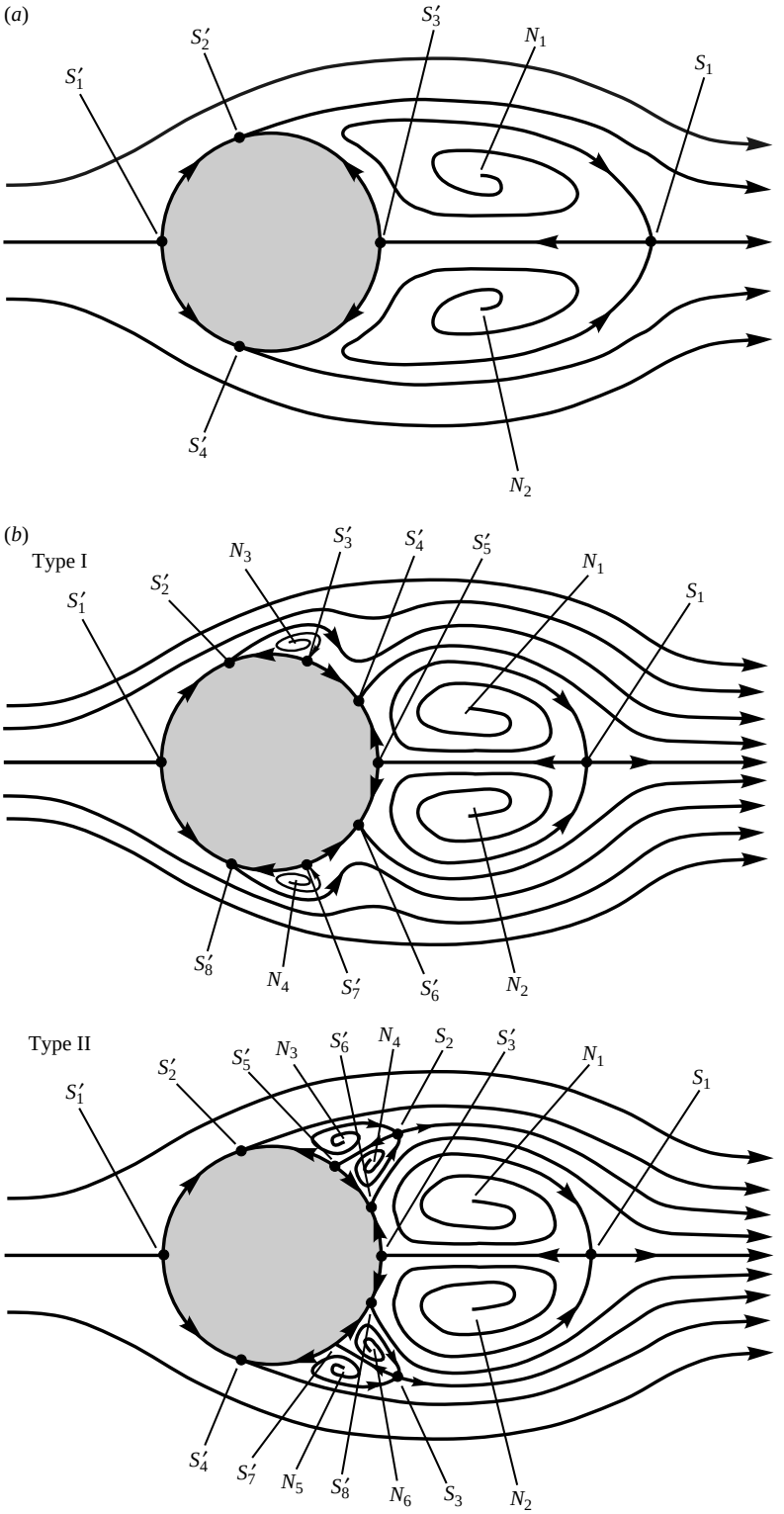

FIGURE 7. Topological flow patterns of a natural circular cylinder for flow with three-dimensional effect. (*a*) Laminar separation for $Re_D < 0.55 \times 10^5$. (*b*) Separation bubble for $Re_D > 0.55 \times 10^5$.

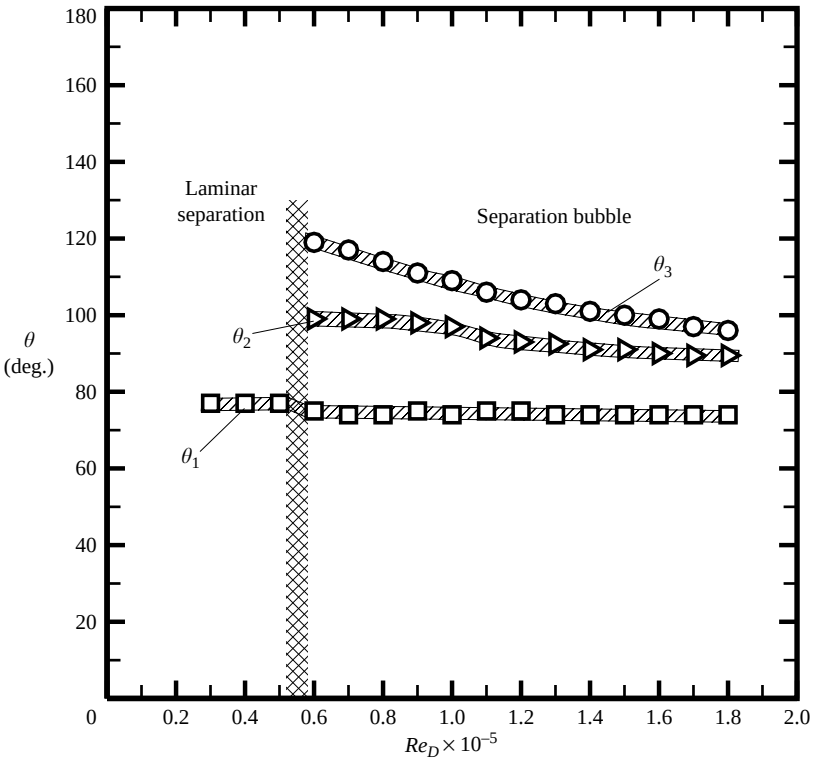

FIGURE 8. Variations of characteristic angles on the surface of a natural circular cylinder in the subcritical regime.

0.5×10^5. Figures 9(*a*) and 9(*b*) show the situations when the control rod is placed at $\alpha = 67.5^\circ$ and 72°, respectively, which are in the region upstream of the natural separation angle ($\theta_1 \approx 77^\circ$). In both pictures, the surface oil-flow displays a pattern of two dark strips, which is quite different from the single dark strip pattern of figure 5(*b*). In figure 9(*a*), the upstream dark strip is located at $\theta_1 \approx 71^\circ$, which is much smaller than the natural separation angle, whereas in figure 9(*b*), the upstream dark strip is located at $\theta_1 \approx 77.5^\circ$, which is about the same as angle the natural separation angle. The flow direction between these two dark strips, identified by using the TiO_4 method, shows bi-directional characteristics similar to those observed in figures 5(*c*) and 5(*d*), as marked by the arrowheads in figure 9(*a*). A three-way saddle must exist between the upstream- and downstream-going flows, although the oil does not accumulate there to form a visible dark strip owing to the depletion effect of the divergent flows. Experiments conducted at other Reynolds numbers in the subrange $Re_D < 0.55 \times 10^5$ for the control rod angles $\alpha < 77^\circ$ show similar results. The effect on the boundary layer induced by placing the vibrating rod in the region upstream of the natural separation point in the low-Reynolds-number subrange $Re_D < 0.55 \times 10^5$ seems to push the separation mode to that which exists on the natural cylinder in the high-Reynolds-number subrange: the surface flow mode shifts from the laminar separation (which occurs at $Re_D < 0.55 \times 10^5$) to the separation bubble (which occurs at $Re_D > 0.55 \times 10^5$). Figures 9(*c*) and 9(*d*) show the oil patterns when the control rod is placed at $\alpha = 77^\circ$ and 81°, respectively, which are located at or downstream of the separation angle ($\theta_1 \approx 77^\circ$) of the natural cylinder flow. A single dark strip appears

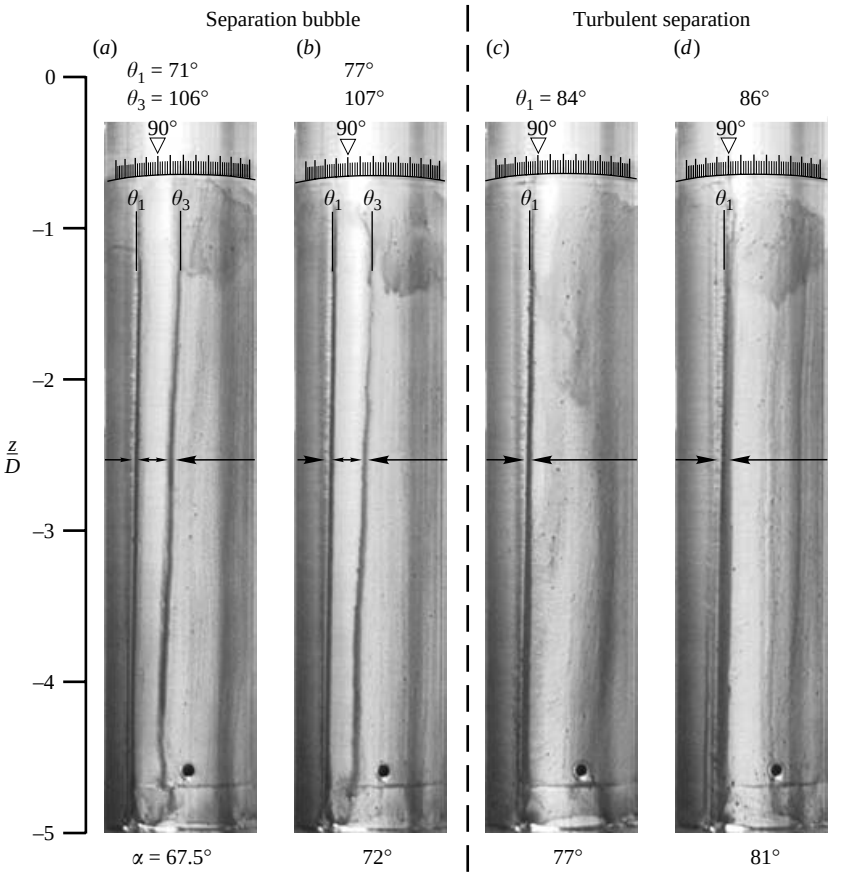

FIGURE 9. Surface oil-flow patterns of a modulated circular cylinder at $Re_D = 0.5 \times 10^5$. (*a*) $\alpha = 67.5°$, (*b*) 72°, (*c*) 77°, (*d*) 81°.

on both figures. The flow directions, as marked in the figures, show that the surface boundary layers simply separate. The separation angles θ_1 in figures 9(*c*) and 9(*d*) are 84° and 86°, respectively. With the excitation of the vibrating rod located at angle $\alpha \geqslant 77°$, the effect on the surface flow is apparent: the surface flow changes from the laminar separation mode to the turbulent separation mode and the separation point is postponed a little downstream. It is apparent that in order to defer the separation angle in the subrange of $Re_D < 0.55 \times 10^5$ with the technique of the vibration rod, the rod should be placed at or downstream of the natural separation angle.

Figure 10 shows the oil flow on the surface of the circular cylinder under the modulation of the vibrating rod at Reynolds number $Re_D = 1.3 \times 10^5$. The control rod is placed upstream, on the spot, or downstream of the natural separation angle (74°) of the separation bubble mode. For all cases, the modulated surface flow becomes the turbulent separation mode since only a single dark strip appears on the cylinder surface. The oil-accumulated dark strip is not as sharp as those observed in figure 9 because the induced turbulence is stronger when the boundary layer is excited at this high Reynolds number. The separation angles $\theta_1 = 126°$, 130° and 134° correspond to the rod angles $\alpha = 72°$, 74° and 81°, respectively. No matter whether the vibrating rod is placed upstream or downstream of the natural separation angle, the flow mode is modulated and the separation point is deferred greatly to the downstream area.

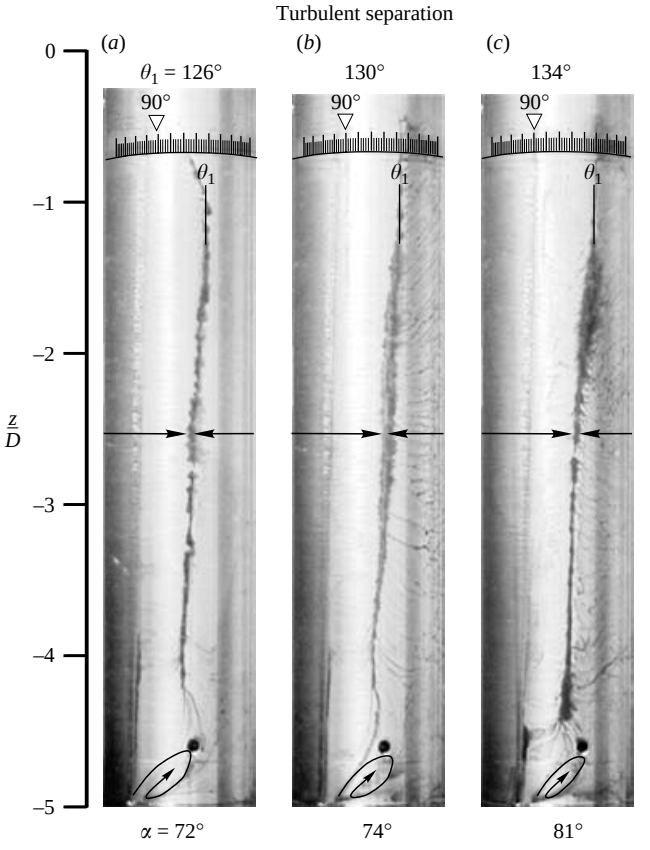

FIGURE 10. Surface oil-flow patterns of a modulated circular cylinder at $Re_D = 1.3 \times 10^5$. (*a*) $\alpha = 72°$, (*b*) 74°, (*c*) 81°.

Placing the control rod downstream of the natural separation point can even postpone the separation point to the far downstream area at 134°. All experiments conducted at other Reynolds numbers in the subrange of $Re_D > 0.55 \times 10^5$ show similar results. It is apparent that in the high-Reynolds-number subrange $Re_D > 0.55 \times 10^5$, placing the vibrating rod downstream of the natural separation point can postpone the separation point to the downstream region farther than that induced by placing the rod upstream of the natural separation point.

Figure 11 shows the variation of the separation angle θ_1 with the control angle α at various Reynolds numbers. At all Reynolds numbers, the separation point moves downstream with increasing control angle. Placing the control rod upstream of the separation angle of the natural cylinder causes a larger increase rate than placing it at positions downstream of the separation angle of the natural cylinder. In the subrange of $Re_D < 0.55 \times 10^5$, the vibration excitation in the separated boundary layer downstream of the natural separation angle ($\theta_1 = 77°$) would never cause the separation point to move downstream farther than 90°. However, in the subrange of $Re_D > 0.55 \times 10^5$, applying the vibration excitation to the separated boundary layer of the natural cylinder could delay the separation point from $\theta_1 = 74°$ to the far downstream area between 110° and 140°. This may be because the turbulence induced by the rod vibration in the low-Reynolds-number subrange is still incapable of exceeding a threshold to overcome the barrier of the viscous effect.

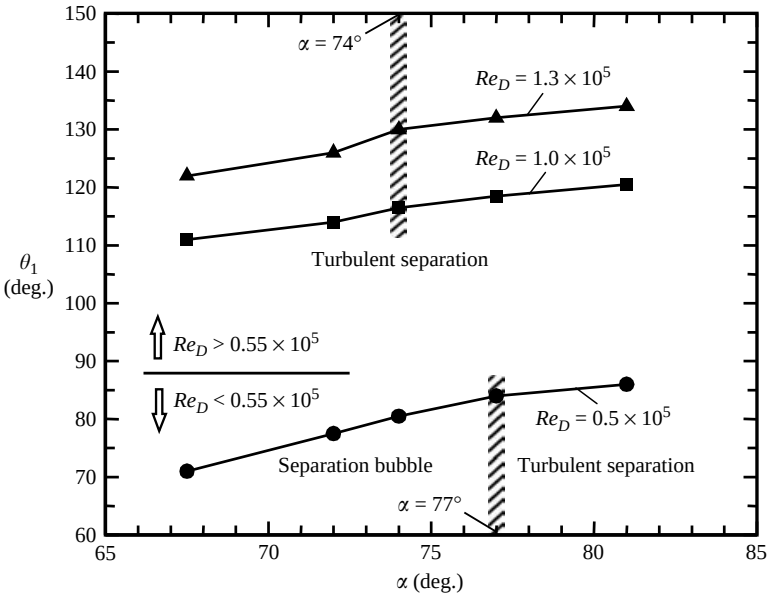

FIGURE 11. Variations of the separation angle θ_1 with control angle α at various Reynolds numbers.

A discussion on the natural and the controlled characteristic flow modes follows. The separation bubble mode is observed in the natural boundary layer of the circular cylinder in the high-Reynolds-number subrange or in the upstream-agitated (agitation at locations upstream of the natural separation point) boundary layer of the circular cylinder in the low-Reynolds-number subrange. In these situations, the turbulence kinetic energy in the boundary layer assists in the inertial force to counterbalance the local adverse pressure gradient to attain a critical condition that the separated boundary layer can reattach to the cylinder surface and form secondary recirculation bubbles, i.e. the increased momentum mixing due to the enhanced turbulence intensity makes the boundary layer susceptible to reattaching to the surface. This physical mechanism and phenomenon are similar to that which occurs on the low-Reynolds-number airfoil reported by many investigators (e.g. O'Meara & Mueller 1987; Huang & Lin 1995). When the flow passes over an airfoil at a Reynolds number between 10^4 and 10^6 at moderate angle of attack, the separated laminar boundary layer may reattach to the suction surface of the airfoil because the adverse pressure gradient induced by the streamlined profile of the airfoil would not be drastically large.

If the turbulence kinetic energy in the boundary layer is high enough to overcome the local adverse pressure gradient by some means, e.g. agitation in the high-Reynolds-number subrange or excitation at the downstream region of the natural separation point in the low-Reynolds-number subrange, the increased mixing enables the boundary layer to withstand a high adverse pressure gradient and, as a consequence, the separation is delayed, i.e. the separation point is pushed downstream and the turbulent separation occurred thereafter. Norberg & Suden (1987) reported that the separation point at $Re_D = 2 \times 10^5$ is about 105°, which can serve as a physical definition of the boundary between the subcritical and the (pre)critical regimes, if the turbulence intensity embedded in the free stream is 0.1 %. They also found that the separation angle can be deferred downstream to around 125° if the free stream turbulence intensity is increased to 1.4 %. The effect of the turbulence on the

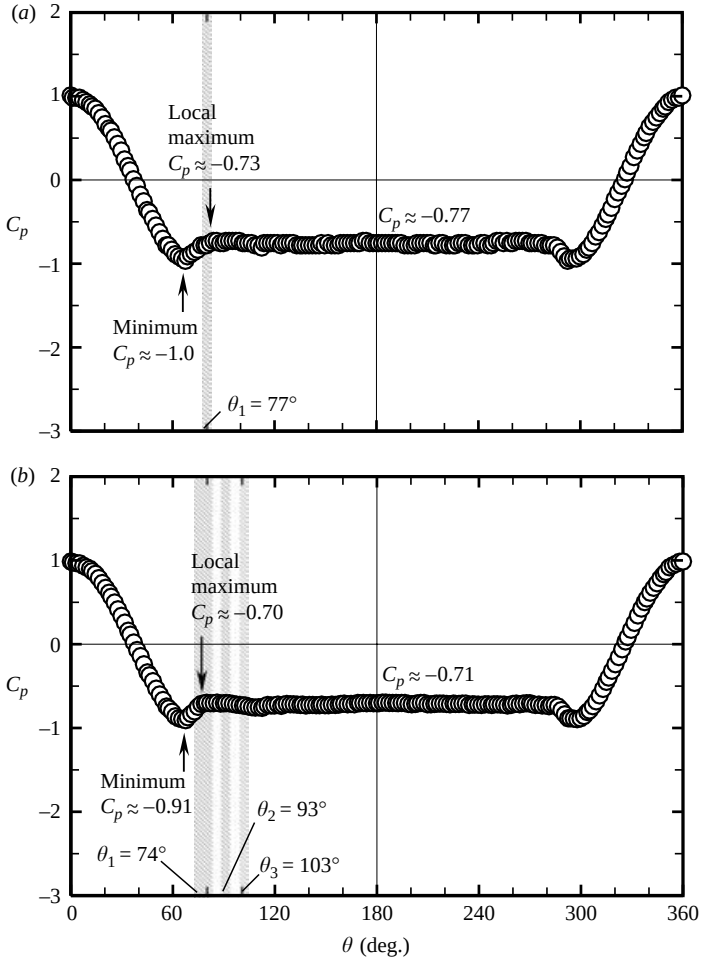

FIGURE 12. Pressure coefficients C_p of a natural circular cylinder at (*a*) $Re_D = 0.5 \times 10^5$, (*b*) $Re_D = 1.3 \times 10^5$.

boundary-layer behaviour is obvious. Therefore, the separation bubble mode can be taken as a state of transition between the extreme states of laminar separation and turbulent separation.

3.4. *Surface pressure characteristics*

Figures 12(*a*) and 12(*b*) show the measured distributions of the surface pressure coefficient C_p at Reynolds numbers 0.5×10^5 and 1.3×10^5, respectively. The pressure coefficient is defined as $C_p \equiv (p - p_{fs})/(\rho u^2/2)$, where p denotes the measured local static pressure of the cylinder surface, p_{fs} is the static pressure of the free stream, ρ is the density of the free stream, and u is the free stream velocity. Both distributions are typical and similar to those obtained by previous investigators. The distribution curves are symmetric about $\theta = 180°$. The pressure coefficient C_p decreases from unity at the forward stagnation point ($\theta = 0°$) to the minimum values about -1 (for $Re_D = 0.5 \times 10^5$) and -0.91 (for $Re_D = 1.3 \times 10^5$) at $\theta \approx 67.5°$ and $66.5°$, respectively. The pressure coefficient C_p increases gradually with the increase of θ to a local maximum located around the separation point (77° for $Re_D = 0.5 \times 10^5$

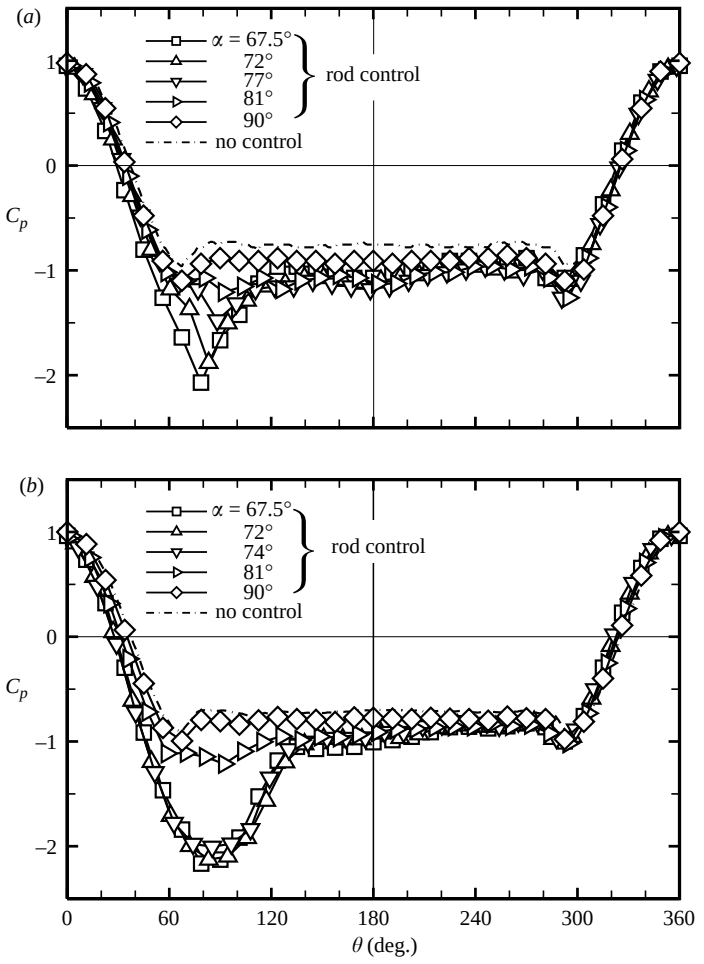

FIGURE 13. Pressure coefficients C_p of a vibrating rod-controlled circular cylinder at (*a*) $Re_D = 0.5 \times 10^5$, (*b*) $Re_D = 1.3 \times 10^5$.

and 74° for 1.3×10^5), then decreases a little, and remains almost constant thereafter in the region covered by the recirculation bubble. The base pressure coefficients in the region $\theta \approx 80° - 280°$ are about -0.77 and -0.71 for $Re_D = 0.5 \times 10^5$ and 1.3×10^5, respectively. C_p increases from the minimum to the local maximum located around the separation point because the flow velocity in the attached boundary layer upstream of the separation point must decelerate before it approaches the separation point. After the separation, the surface pressure decreases inappreciably and remains almost at a constant level. Because the boundary-layer separation point at $Re_D = 1.3 \times 10^5$ is 74°, which is earlier than $\theta = 77°$ at $Re_D = 0.5 \times 10^5$, the increase of the pressure from the minimum value occurring at $Re_D = 1.3 \times 10^5$ is earlier than that occurring at $Re_D = 0.5 \times 10^5$. The minimum value and the base pressure coefficient of $Re_D = 1.3 \times 10^5$ are thus larger than those of $Re_D = 0.5 \times 10^5$.

When the main cylinder is subject to the excitation of the vibrating rod, the pressure coefficient presents complex behaviours other than the natural cylinder flow. Figure 13(*a*) shows the situation occurring at $Re_D = 0.5 \times 10^5$. At this Reynolds number, excitation on the boundary layer at the regions upstream of the natural

separation point ($\theta = 77^\circ$) will force the boundary layer to separate and reattach subsequently to form the secondary separation bubble, as illustrated in figures 9(*a*) and 9(*b*). The separation point moves downstream and the bubble length shortens with increasing control angle α. For instance, the separation point is located at $\theta = 71^\circ$ when $\alpha = 67.5^\circ$ and is at $\theta = 77.5^\circ$ when $\alpha = 72^\circ$. The bubble covers the area from the separation point to about 106° for both cases. The surface pressure in the bubble region is lower than the free-stream pressure because of the flow recirculation. A long bubble would occupy a wide low-pressure area. Therefore, the pressure coefficient distribution for $\alpha = 67.5^\circ$ has a minimum C_d down to -2.1 which is lower than the value -1.85 for $\alpha = 72^\circ$ because the bubble for $\alpha = 72^\circ$ is shorter than that for $\alpha = 67.5^\circ$. Therefore, the secondary bubble induced by the vibration rod placed at the positions upstream of the natural separation point in the low-Reynolds-number subrange would apparently increase the lift. Both the values of the minimum C_p and the θ angle corresponding to the minimum C_p increase when the control angle moves to the downstream area because the bubble shortens and the separation point moves downstream. For $\alpha = 77^\circ$ and 81°, the turbulent separation occurs at $\theta = 84^\circ$ and 86°, respectively, which are further downstream than those of the separation bubble mode when $\alpha = 67.5^\circ$ and 72°. Disappearance of the bubble naturally is beneficial for the increase of surface pressure. Both the minimum C_p value and the corresponding θ angle of the minimum C_p thus increase further because the boundary layer simply separates and the separation point moves downstream to $\theta = 84^\circ$ and 86°, respectively. As the control rod is placed at $\alpha = 90^\circ$, the influence of intensification in turbulence induced by the rod vibration becomes less significant when compared with that of the upstream situation, therefore the separation angle would move a little upstream (compared with 77° for the natural cylinder) to about 75°. Hence, the pressure coefficient presents an almost similar profile to that of no control, except that the C_d values are a little lower.

If the Reynolds number is in the subrange $Re_D > 0.55 \times 10^5$, the pressure coefficient of the controlled cylinder presents different behaviours. In this regime, the natural separation point is 74°. It is deferred far downstream if the vibrating rod is applied, as shown in figure 11. The surface flow is forced to the turbulent separation mode from the separation bubble mode since the strong turbulence is triggered in the boundary layer by the agitation of the vibrating rod. From the potential flow theory, the pressure coefficient should continuously decrease from unity at $\theta = 0^\circ$ down to -3 at $\theta = 90^\circ$, and then increase subsequently to unity again at $\theta = 180^\circ$. If the control rod is placed at the positions upstream of the natural separation point of 74°, as shown in figure 13(*b*), owing to the agitation of the rod vibration, the flow in the boundary layer upstream of the separation point is highly turbulent and the turbulence kinetic energy attains a level at which it can overcome the adverse pressure gradient in the downstream area. The boundary layer, therefore, can attach to the cylinder surface even in the far downstream area. In the region of the attached boundary layer, downstream of the reattachment point, the pressure decreases continuously with the increase of θ until it attains the minimum value at $\theta \approx 90^\circ$ and increases thereafter because of momentum conservation. When the flow approaches the separation point, the deceleration in velocity makes the pressure increase, so that a minimum C_p is observed. For instance, for control angle $\alpha = 67.5^\circ$, 72° and 74°, the pressure coefficient profiles are lowered to about -2.17 at $\theta = 78.75^\circ$, -2.13 at $\theta = 83.25^\circ$ and -2.01 at $\theta = 85.25^\circ$, respectively, then rise from the minima subsequently to local maxima around the separation points of $\theta = 122^\circ$, 126° and 130°. When the control rod is placed at a position downstream of the natural separation point $\alpha = 74^\circ$, e.g.

$\alpha = 81°$, the effect of lowering the pressure coefficient is not as significant as that of placing the rod upstream of the natural separation point. Therefore, the vibration agitation at positions upstream of the natural separation point in the high-Reynolds-number subrange could effectively increase the lift. In the uncontrolled case, it would decrease to a minimum at somewhere upstream of the natural separation point and go up subsequently to somewhere around the natural separation point. However, in the case of downstream excitation, the pressure coefficient profile behaves similarly to the uncontrolled case in the region upstream of the natural separation point. The turbulence level upstream of the control angle is not as large as that in the downstream area. Therefore, the pressure profile goes up a little and is quickly lowered to a minimum of -1.22 at $\theta = 91.8°$, then increases to a local maximum around the separation point $\theta = 134°$.

In short, the modulation on the surface flow patterns can significantly influence the surface pressure distributions on the main cylinder. The pressure coefficient of the natural cylinder decreases from unity at the stagnation point to a minimum located upstream of the separation point, increases to a local maximum around the separation point, and subsequently remains at an almost constant level in the reverse flow region. Modulating the boundary layer, either from the laminar separation mode to the separation bubble mode in the low-Reynolds-number subrange or from the separation bubble mode to the turbulent separation mode in the high-Reynolds-number subrange, by applying the vibrating rod upstream of the natural separation point will drastically lower the values of the minimum pressure coefficient and the base pressure coefficient. However, modulating the boundary layer to the turbulent separation mode by placing the vibrating rod downstream of the natural separation point in the low-Reynolds-number subrange or in the high-Reynolds-number subrange will only lower the minimum pressure coefficient and the base pressure coefficient by insignificant values when compared with the characteristics of the natural cylinder. Because both the minimum pressure coefficient and the base pressure coefficient are decreased, apparent drag reduction by using the vibrating rod technique in the cylinder flow would not be expected. However, forcing the boundary layer at the positions upstream of the natural separation point in the subcritical regime would drastically increase the lift.

3.5. *Wake instability characteristics*

The influence of the rod vibration on the vortex-shedding characteristics in the cylinder wake is complex. It depends on the relative positions of the control rod and the separation point as well as the ranges of the Reynolds number.

Figure 14 shows the time series of the velocity signals measured at three positions in the near wake (detected by a hot-wire anemometer) at $Re_D = 0.5 \times 10^5$ and the corresponding power spectrum density functions Φ. The power spectrum density function Φ is the distribution of 'energy density' with frequency. Its dimension is the energy per unit mass per frequency. Integrating Φ over a frequency range would give the total energy content within that frequency range. The mathematical definition is given as $\int_0^\infty \Phi(\omega)\,\mathrm{d}\omega = \lim_{T\to\infty} \int_0^\infty u^2(t)\,\mathrm{d}t$, where u is the instantaneous velocity digitized by the high-speed data acquisition system, ω is the frequency, t is the evolving time, and T is the period of integration. The mathematical definition can be transformed into an arithmetic form by using the fast Fourier transform (FFT) algorithm so that the time consumption in converting the raw data from the time domain to the frequency domain is greatly shortened. In figure 14(a), typical vortex-shedding signals in the wake of a natural circular cylinder are shown: periodic

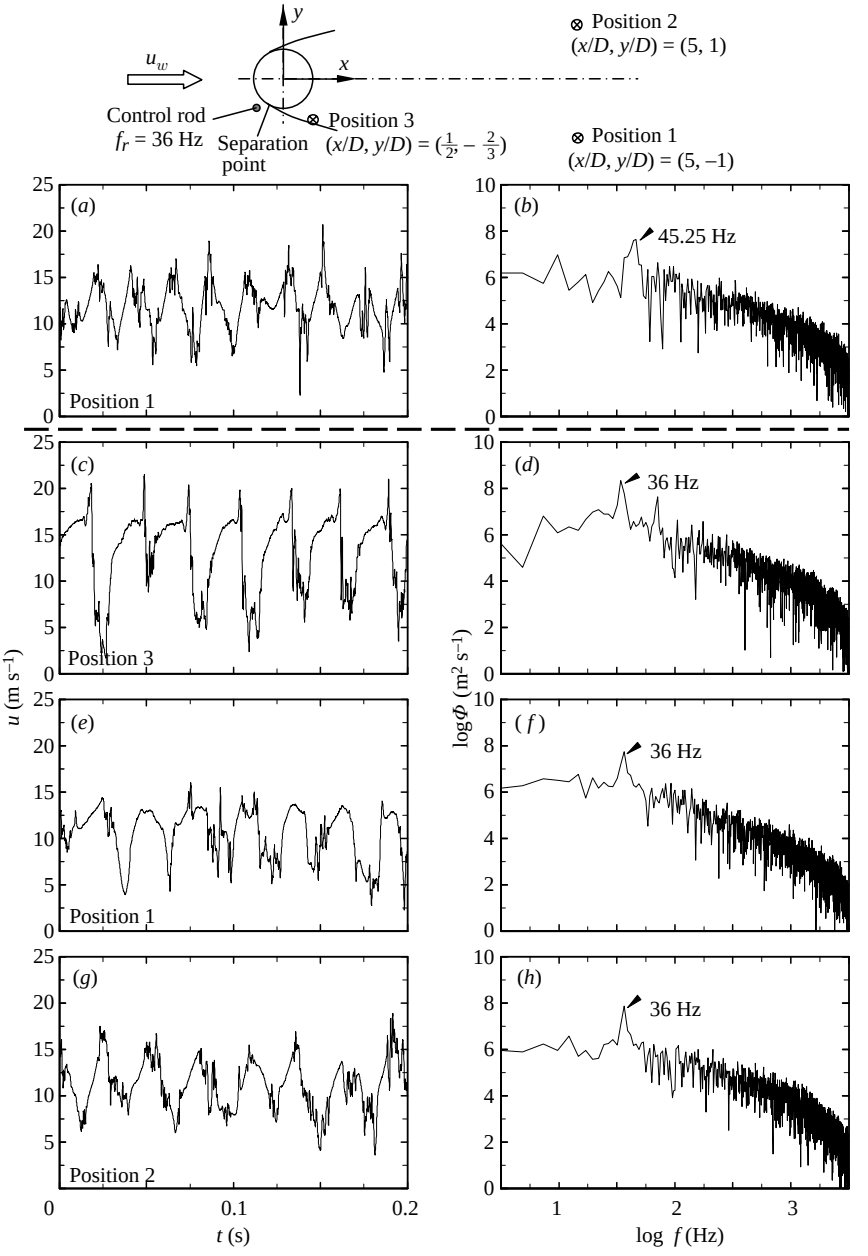

FIGURE 14. Time histories of velocity signals u and the corresponding power spectrum density functions Φ in the wake of a circular cylinder at $Re_D = 0.5 \times 10^5$ and $\alpha = 72°$. (a, b) Natural cylinder, $(c–h)$ vibrating rod-controlled cylinder.

signals superimposed by fluctuations. The vortex shedding of the natural cylinder is detected at five cylinder diameters downstream of the forward stagnation point, as marked by 'Position 1' in figure 14. The vortex-shedding frequency of this natural state is $f_s = 45.25$ Hz, as indicated in the peak value of the corresponding power spectrum density function of figure 14(b). As the control rod is placed at the angle $\alpha = 72°$, which is in the region upstream of the natural separation point (77°), the velocity

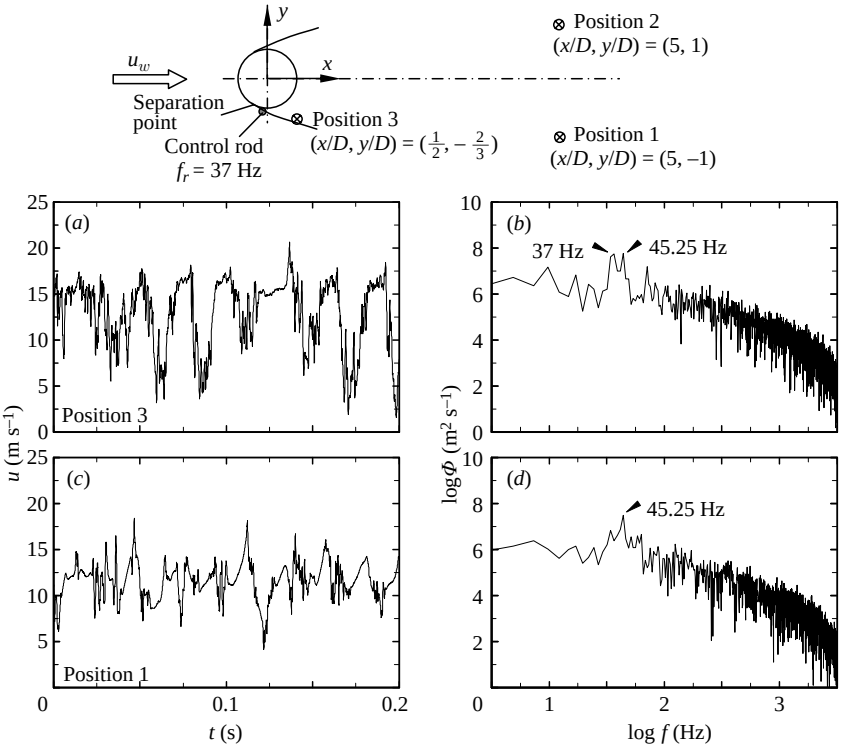

FIGURE 15. Time histories of velocity signals u and corresponding power spectrum density functions Φ in the wake of a vibrating-rod-controlled circular cylinder at $Re_D = 0.5 \times 10^5$ and $\alpha = 81^\circ$.

signals measured at 'Position 3' are greatly modulated, as shown in figure 14(c). A peak appears at the end of each wave period because the measuring position is near the separated boundary layer, and large fluid motion induced by the rod vibration surges over the hot-wire sensor. As shown in figure 14(d), the frequency shifts from the natural shedding frequency 45.25 Hz to 36 Hz $= f_r$, where f_r is the vibration frequency of the control rod. The original shedding frequency disappears. For measurements at the 'Position 1', which is in the downstream area and on the same side of the control rod, the peaks appearing in figure 14(c) become faded, as shown in figure 14(e). The detected frequency of vortex shedding is still the same as the frequency of the rod vibration, as shown in figure 14(h). Measurements taken at 'Position 2', which is on the opposite side of the control rod, reveal that the velocity signals are not significantly modulated by the vibration motion of the control rod, as shown in figure 14(g). The velocity signals in figure 14(g) are more similar to those in figure 14(a), and less similar to those in figures 14(c) and 14(e). However, the vortex-shedding frequency is still modulated by the rod vibration to 36 Hz $= f_r$.

As the control rod is placed at angle $\alpha = 81^\circ$, which is in the region downstream of the natural separation point (77°), the velocity signals measured at 'Position 3' are shown in figure 15(a). Obviously, the periodic signals are superimposed by strong fluctuations. There are two peaks in figure 15(b): one appears at the frequency that is equal to the natural vortex-shedding frequency of 45.25 Hz and the other appears at the rod vibration frequency of 37 Hz. Unlike the situation in figure 14(d), the flow in figure 15(b) possesses bi-frequency characteristics. In the downstream area, the

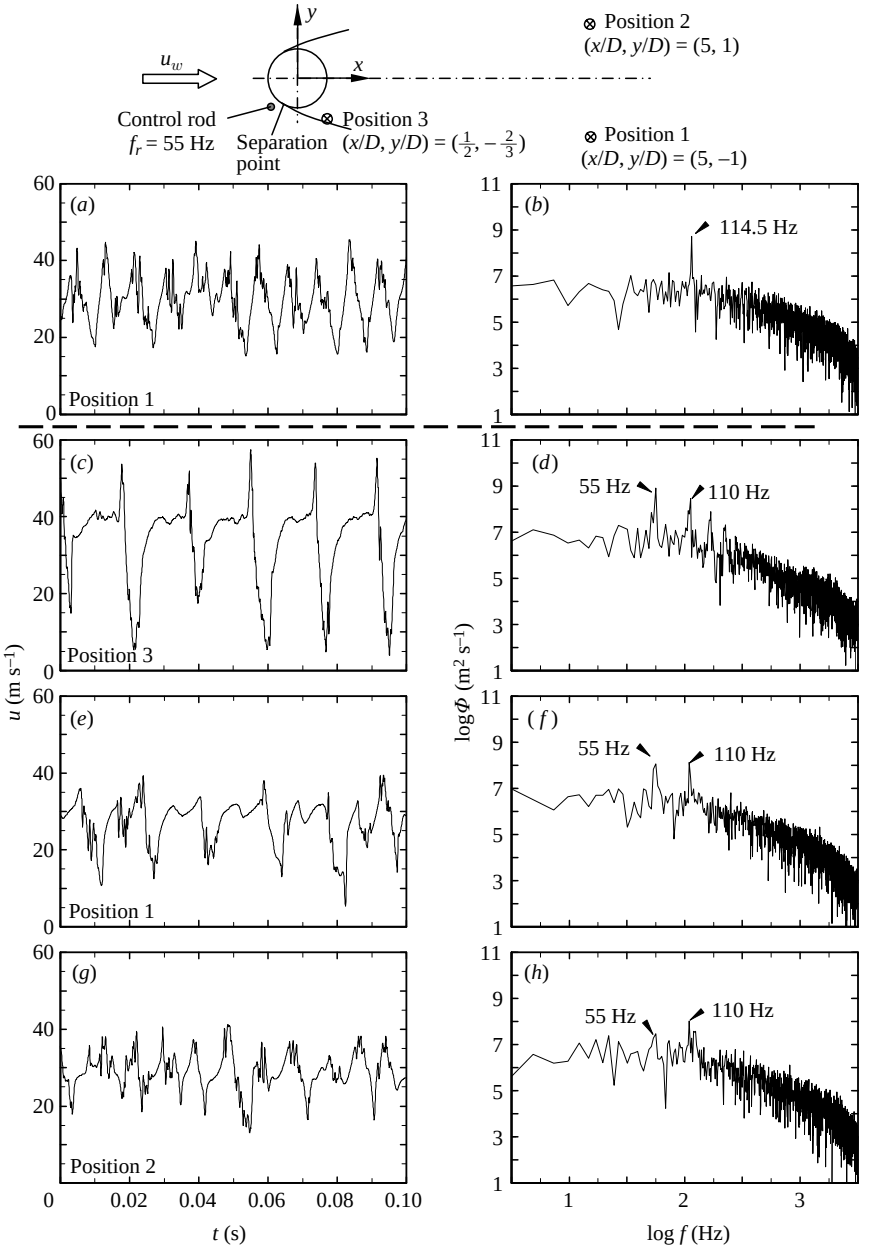

FIGURE 16. Time histories of velocity signals u and corresponding power spectrum density functions Φ in the wake of a circular cylinder at $Re_D = 1.3 \times 10^5$ and $\alpha = 72°$. (a, b) Natural cylinder, (c–h) vibrating rod-controlled cylinder.

measurement at 'Position 1' shows a peak at the natural shedding frequency 45.25 Hz only, i.e. the vortex-shedding frequency is not modulated by the rod vibration. The measurements at 'Position 2' are not shown here because they are similar to those in figures 14(a) and 14(b).

Figure 16 shows the time series of the velocity signals and the corresponding power spectrum density functions Φ at $Re_D = 1.3 \times 10^5$. Figures 16(a) and 16(b) show typical vortex-shedding signals in the wake of a natural circular cylinder

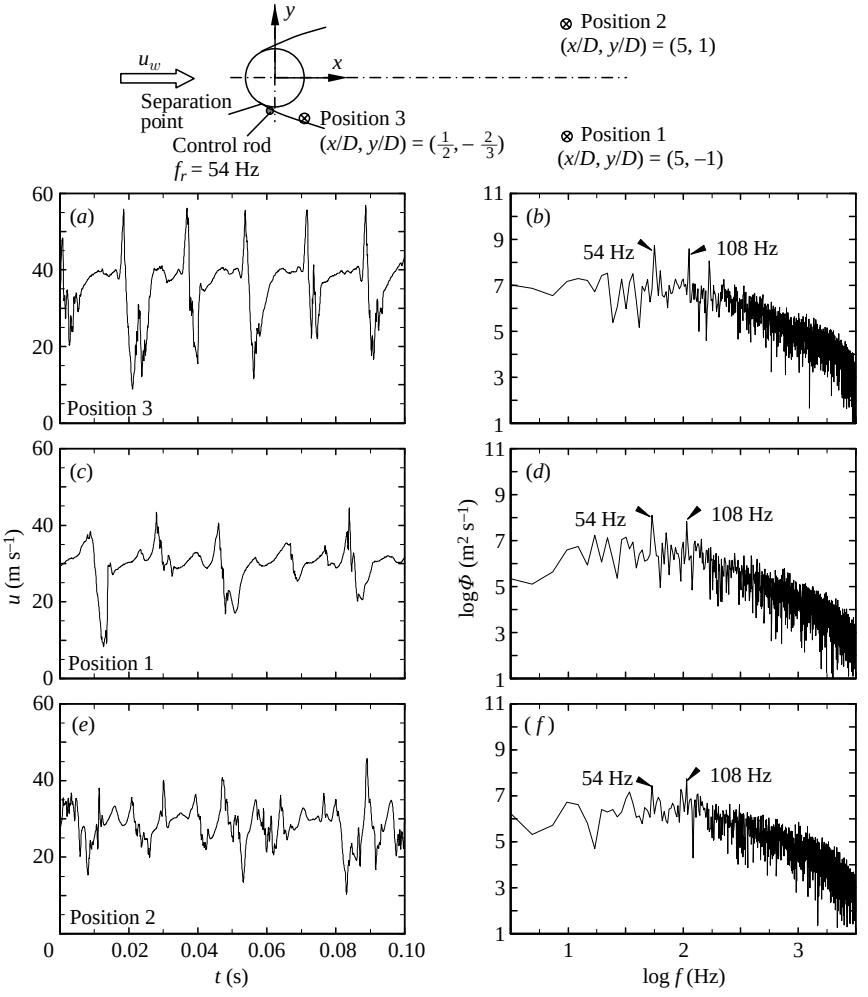

FIGURE 17. Time histories of velocity signals u and corresponding power spectrum density functions Φ in the wake of a vibrating-rod-controlled circular cylinder at $Re_D = 1.3 \times 10^5$ and $\alpha = 81^\circ$.

and a peak appearing at a frequency of 114.5 Hz. As the control rod is placed at angle $\alpha = 72^\circ$, which is in the region upstream of the natural separation point (74°), the velocity signals measured at 'Position 3' are modulated greatly by the vibrating rod, as shown in figure 16(c), and look similar to those observed in figure 14(c). In the frequency domain, as shown in figure 16(d), dual peaks are observed: at the rod vibration frequency 55 Hz and the other at 110 Hz which is the second harmonic of 55 Hz. The natural vortex-shedding frequency disappears when rod vibration is applied. Measurements taken in the downstream area ('Position 1' and 'Position 2') show a similar situation of dual-frequency characteristics, as shown in figures 16(e)–16(h). The appearance of the second harmonic is natural because the periodic signals, as shown in figures 16(c), 16(e) and 16(g), contain asymmetric half waves in a complete wave. The modulation in the waveforms is induced by strong vibration of the control rod. As the control rod is placed at angle $\alpha = 81^\circ$, which is in the region downstream of the natural separation angle, the modulated frequency characteristics of vortex shedding, as shown in figures 17(a) to 17(f), are similar to those presented in figures 16(c)–16(h).

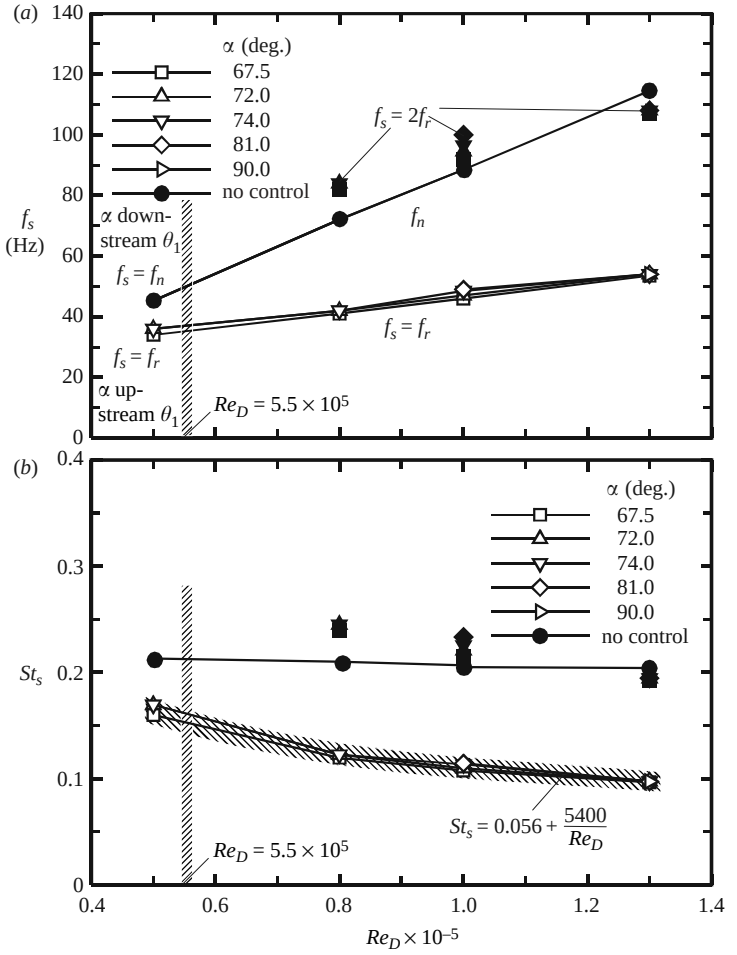

FIGURE 18. (*a*) Variations of vortex-shedding frequency f_s and (*b*) corresponding Strouhal number St_s, with Reynolds number Re_D.

Figure 18 shows the frequency f_s (figure 18*a*) and the corresponding Strouhal number St_s (figure 18*b*) of the vortex shedding in the wake. The vortex shedding frequency of the natural circular cylinder (f_n) increases almost linearly with increasing Reynolds number. Its counterpart of the Strouhal number in figure 18(*b*) remains almost constant at about 0.21. Careful examination of the Strouhal number of natural vortex shedding would find that St_s decreases slightly in an insignificant way with increasing Reynolds number. This phenomenon can be observed in almost all previous of investigations. This may be induced by the increase of turbulence intensity when the Reynolds number is increased (Huang & Lee 2000). Because the entrainment of the vortices would increase with the increase in turbulence intensity, the length and time scales of the vortices may therefore increase a little. This may retard the rate of frequency increase when the Reynolds number is increased. The Strouhal number would thus decrease with the increasing Reynolds number. In figure 18(*a*), in the subrange of $Re_D < 0.55 \times 10^5$, all the vortex-shedding frequencies are modulated to the frequency of the rod vibration if the control rod is placed in the region upstream of the natural separation point. If the control rod is placed downstream

of the natural separation point, no effect on the vortex-shedding frequency would be observed. In the subrange of $Re_D > 0.55 \times 10^5$, all the vortex-shedding frequencies of the controlled flow are modulated towards the corresponding vibration frequencies of the control rod (accompanied by apparent second harmonics), no matter whether the rod is placed up- or downstream of the natural separation point. The corresponding Strouhal number of the controlled vortex-shedding frequency is shown in figure 18(*b*). A fitted curve is provided for convenience of application.

4. Summary and conclusions

The results of the experimental investigation presented in this paper provide new and additional information concerning the natural and the vibrating-rod-controlled flow properties around a circular cylinder in crossflow. A technique of inducing self-vibration of an elastic rod is successfully developed by using the principle of galloping. The surface flow, pressure distribution and vortex-shedding characteristics of a circular cylinder in the subcritical regime can be modulated by using the self-excited vibrating rod which is placed near the natural boundary-layer separation point. The mechanism of causing the elastic rod to vibrate is passive and the effective Reynolds-number range of this control method is wide so that the application to the boundary-layer control of the objects of various shapes is possible. For example, it would be worth investigating the effectiveness of applying this self-excited vibrating-rod technique to controlling the boundary-layer separation and the wake instability of the airfoil.

The surface flow of the natural circular cylinder in the subcritical regime presents distinctly different appearances in two Reynolds-number subranges: $Re_D < 0.55 \times 10^5$ and $Re_D > 0.55 \times 10^5$. The laminar separation mode is found in the low-Reynolds-number subrange, while the separation bubble mode is observed in the high-Reynolds-number subrange. In the vibrating-rod-controlled case, the flow may be modulated to the separation bubble mode or the turbulent separation mode, which depend on the Reynolds-number subrange and the control angle at which the control rod is positioned. The separation angle of the turbulent separation mode induced by the rod vibration can be postponed to the far downstream area (even larger than 130°) because the induced turbulence kinetic energy is strong enough to overcome the adverse pressure gradient in the downstream region. The separation bubble mode (observed either in the natural boundary layer in the high-Reynolds-number subrange or in the upstream-agitated boundary layer in the low-Reynolds-number subrange), which is formed owing to the reattachment of the separated boundary layer, is induced by the turbulence kinetic energy generated in the separated boundary layer. It could be taken as a state of transition between the laminar separation and the turbulent separation. Modulation on the surface flow patterns could significantly influence the surface pressure distributions on the circular cylinder.

Forcing the boundary layer to the separation bubble mode in the low-Reynolds-number subrange or to the turbulent separation mode would drastically lower the values of the minimum pressure coefficient and the base pressure coefficient. Because both the minimum pressure coefficient and the base pressure coefficient are decreased, apparent drag reduction by using the vibrating rod technique in the cylinder flow would not be significant. However, it would drastically increase the lift. The rod vibration could also influence the vortex-shedding frequency in the cylinder wake. The vibration of the control rod could make the vortex shedding in the wake 'lock' to the vibration frequency of the rod if the rod is placed at the proper position in the

region upstream of the natural separation point in the low-Reynolds-number subrange or in the region around the natural separation point in the high-Reynolds-number subrange.

REFERENCES

Achenbach, E. 1968 Distribution of local pressure and skin friction around a circular cylinder in cross-flow up to $Re = 5 \times 10^6$. *J. Fluid Mech.* **34**, 625–639.

Ahlborn, F. 1902 Über den mechanismus des hydro-dynamischen widrstandes. *Abh. Geb. Naturwiss.* **17**.

Alam, M. M., Moriya, M., Takai, K. & Sakamoto, H. 2003 Fluctuating fluid forces acting on two circular cylinders in tandem arrangement at a subcritical Reynolds number. *J. Wind Engrs Indust. Aerodyn.* **91**, 139–154.

Ballengee, D. & Chen, C. F. 1971 Experimental determination of the separation point of flow around a circular cylinder. *Flow, its Measurement and Control in Science and Industry, vol. 1, Proc. ASME Fluids Engineering Conference on Flow Characteristics* (ed. R. B. Dowell), pp. 419–427. Instrument Society of America, Pittsburgh.

Bearman, P. W. 1969 On vortex shedding from a circular cylinder in the critical Reynolds number regime. *J. Fluid Mech.* **37**, 577–585.

Blevin, R. D. 1990 *Flow-Induced Vibration*, pp. 43–103. Van Nostrand Reinhold.

Bouard, R. & Coutanceau, M. 1980 The early stage of development of the wake behind an impulsively started cylinder for $40 < Re < 10^4$. *J. Fluid Mech.* **160**, 93–117.

Chong, M. S. & Perry, A. E. 1990 A general classification of three-dimensional flow fields. *Phys. Fluids* A **2**, 765–777.

Den Hartog, J. P. 1956 *Mechanical Vibrations*, pp. 228–245. McGraw-Hill.

Dowell, E. H. 1978 *A Modern Course in Aeroelasticity*, pp. 281–325. Sijthoff, The Netherlands.

Fage, A. & Falkner, V. M. 1931 Further experiments on the flow around a circular cylinder. *Aero. Res. Counc. Lond. Rep. Mem.* 1369, pp. 1–13.

Farell, C. & Blessmann, J. 1983 On critical flow around smooth circular cylinder. *J. Fluid Mech.* **136**, 375–391.

Fung, Y. C. 1969 *Introduction to the Theory of Aeroelasticity*, pp. 160–185. Dover.

Gölling, B., Dallmann, U. & Kreplin, H. P. 2000 Experimental investigation on active and dynamic instability control of separated turbulent wing/cylinder flows. *European Drag Reduction Conference, Potsdam.*

Huang, R. F. & Lee, H. W. 2000 Turbulence effects on frequency characteristics of unsteady motions in wake of wing. *AIAA J.* **38**, 87–94.

Huang, R. F. & Lin, C. L. 1995 vortex-shedding and shear-layer instability of wing at low-Reynolds numbers. *AIAA J.* **33**, 1398–1403.

Huang, R. F., Shy, W. W., Lin, S. W. & Hsiao, F.-B. 1996 Influence of surface flow on aerodynamic loads of a cantilever wing. *AIAA J.* **34**, 527–532.

Hunt, J. C. R., Abell, C. J., Peterka, J. A. & Woo, H. 1978 Kinematic studies of the flows around free or surface-mounted obstacles: applying topology to flow visualization. *J. Fluid Mech.* **86**, 179–200.

Lee, T. & Basu, S. 1997 Nonintrusive measurements of the boundary layer developing on a single and two circular cylinders. *Exps. Fluids* **23**, 187–192.

Lienhard, J. 1996 *Synopsis of Lift, Drag, and Vortex Frequency Data for Rigid Circular Cylinders.* Technical Extension Service, Washington State University, Bulletin 300.

Merzkirch, W. 1974 *Flow Visualization*, pp. 53–66. Academic.

Nakayama, Y. 1988 *Visualized Flow: Flow Motion in Basic and Engineering Situations Revealed by Flow Visualization.* Oxford University Press.

Niemann, H.-J. & Hölscher, N. 1990 A review of recent experiments on the flow past circular cylinders. *J. Wind Engrs Indust. Aerodyn.* **33**, 197–209.

Nishimura, H. & Taniike, Y. 2001 Aerodynamic characteristics of fluctuating forces on a circular cylinder. *J. Wind Engrs Indust. Aerodyn.* **89**, 713–723.

Norberg, C. 1986 Interaction between free stream turbulence and vortex shedding for a single tube in cross flow. *J. Wind Engrs Indust. Aerodyn.* **23**, 501–514.

Norberg, C. & Sunden, B. 1987 Turbulence and Reynolds number effects on the flow and fluid forces on a single cylinder in cross flow. *J. Fluids Struct.* **1**, 337–357.

O'meara, M. M. & Mueller, T. J. 1987 Laminar separation bubble characteristics on an airfoil at low Reynolds numbers. *AIAA J.* **25**, 1033–1041.

Perry, A. E. & Fairlie, T. R. 1974 Critical points in flow patterns. *Adv. Geophys.* **18**, 299–315.

Perry, A. E. & Steiner, B. D. 1987 Large-scale vortex structures in turbulent wakes behind bluff bodies. Part 1. Vortex formation. *J. Fluid Mech.* **174**, 233–270.

Prasad, A. & Williamson, C. H. K. 1997 A method for the reduction of bluff body drag. *J. Wind Engrs Indust. Aerodyn.* **69–71**, 155–167.

Rao, S. S. 1995 *Mechanical Vibration*, pp. 523–541. Addison-Wesley.

Roshko, A. 1954 On the development of turbulent wakes from vortex streets. NACA Rep. 1191.

Roshko, A. 1961 Experiments on the flow past a circular cylinder at very high Reynolds number. *J. Fluid Mech.* **10**, 345–356.

Sakamoto, H. & Haniu, H. 1994 Optimum suppression of fluid forces acting on a circular cylinder. *Trans. ASME* I: *J. Fluids Engng* **116**, 221–227.

Sakamoto, H., Tan, K. & Haniu, H. 1991 An optimum suppression of fluid forces by controlling a shear layer separated from a square prism. *Trans. ASME* I: *J. Fluids Engng* **113**, 183–189.

Schewe, G. 2001 Reynolds-number effects in flow around more-or-less bluff bodies. *J. Wind Engrs Indust. Aerodyn.* **89**, 1267–1289.

Simpson, A. 1971 On the flutter of a smooth cylinder in a wake. *Aeronaut. Q.* **22**, 25–41.

Son, J. & Hanratty, T. J. 1961 Velocity gradients at the wall for flow around a cylinder at Reynolds numbers from 5×10^3 to 10^5. *J. Fluid Mech.* **35**, 353–368.

Squire, L. C. 1961 The motion of a thin oil sheet under the steady boundary layer on a body. *J. Fluid Mech.* **11**, 161–179.

Strouhal, V. 1878 Über eine besondere Art der Tonerregung. *Annln Phys. Chem.* New Ser. **5** (10), Oct. 216–251.

Strykowski, P. J. & Sreenivasan, K. R. 1990 On the formation and suppression of vortex shedding at low-Reynolds-numbers. *J. Fluid Mech.* **218**, 71–107.

Tsutsui, T. & Igarashi, T. 2002 Drag reduction of a circular cylinder in an air-stream. *J. Wind Engrs Indust. Aerodyn.* **90**, 527–541.

Williamson, C. H. K. 1988 Defining a universal and continuous Strouhal–Reynolds number relationship for the laminar vortex-shedding of a circular cylinder. *Phys. Fluids* **31**, 2742–2744.

Williamson, C. H. K. 1997 Advances in our understanding of vortex dynamics in bluff body wakes. *J. Wind Engrs Indust. Aerodyn.* **69–71**, 3–32.

Zdravkovich, M. M. 1969 Smoke observation of the formation of a Kármán vortex street. *J. Fluid Mech.* **37**, 491–496.

Zdravkovich, M. M. 1981 Review and classification of various aerodynamic and hydrodynamic means for suppressing vortex-shedding. *J. Wind Engrs Indust. Aerodyn.* **7**, 145–189.

Zdravkovich, M. M. 1997 *Flow Around Circular Cylinders*, Oxford University Press.

Zdravkovich, M. M., Brand, V. P., Mathew, G. & Weston, A. 1989 Flow past short circular cylinders with two free ends. *J. Fluid Mech.* **203**, 557–575.